
This is an electronic reprint of the original article.
This reprint may differ from the original in pagination and typographic detail.

Ahmad, W.; Helm, J.; Bossuyt, S.; Reu, P.; Turner, D.; Luan, L. K.; Lava, P.; Siebert, T.; Simonsen, M.

Stereo-DIC Challenge 1.0 – Rigid Body Motion of a Complex Shape

Published in:
Experimental Mechanics

DOI:
[10.1007/s11340-024-01077-7](https://doi.org/10.1007/s11340-024-01077-7)

Published: 01/09/2024

Document Version
Publisher's PDF, also known as Version of record

Published under the following license:
CC BY

Please cite the original version:
Ahmad, W., Helm, J., Bossuyt, S., Reu, P., Turner, D., Luan, L. K., Lava, P., Siebert, T., & Simonsen, M. (2024). Stereo-DIC Challenge 1.0 – Rigid Body Motion of a Complex Shape. *Experimental Mechanics*, 64(7), 1073-1106. <https://doi.org/10.1007/s11340-024-01077-7>

This material is protected by copyright and other intellectual property rights, and duplication or sale of all or part of any of the repository collections is not permitted, except that material may be duplicated by you for your research use or educational purposes in electronic or print form. You must obtain permission for any other use. Electronic or print copies may not be offered, whether for sale or otherwise to anyone who is not an authorised user.



Stereo-DIC Challenge 1.0 – Rigid Body Motion of a Complex Shape

W. Ahmad¹ · J. Helm² · S. Bossuyt¹ · P. Reu³ · D. Turner³ · L.K. Luan⁴ · P. Lava⁵ · T. Siebert⁶ · M. Simonsen⁷

Received: 30 May 2023 / Accepted: 30 April 2024 / Published online: 31 May 2024
© The Author(s) 2024

Abstract

Background Stereo-DIC is a widely used optical measurement technique that provides a dense full-field 3D measurement of the shape, displacement, and strain of a solid sample. When compared with 2D-DIC, Stereo-DIC provides greater flexibility and expands its use beyond flat, planar specimens. Furthermore, the widespread availability of commercial systems has led to the adoption of the technique throughout industry, academia, and government research labs.

Objective Even though some research has been done to understand the effects of different experimental and stereo-DIC parameters, no reference is available to benchmark and compare the performance of current stereo-DIC algorithms to each other.

Methods This paper provides the description and analysis of a carefully controlled 3D experiment and associated images used to compare the results from five subset based DIC software packages. Both the images and analysis codes used in this paper to compare the results are described here and are available for download and use for continued research.

Results We show that over a very large range of motion, the 3D errors are very small, less than $80\mu\text{m}$ over a travel of ± 20 mm out-of-plane and ± 20 mm in-plane. While all codes performed similarly, there are important differences noted in the paper.

Conclusion The image sets and results comparison software are hosted by the International DIC Society (www.iDICs.org) and are freely available for download and analysis for comparison with results in this paper. Furthermore, it is hoped that this set of images can be used for future research in improving stereo-DIC by future authors.

Keywords Stereo-DIC challenge · Metrology · Algorithms comparison · Shape measurement

P. Reu, P. Lava, T. Siebert and J. Helm are the members of SEM.

✉ W. Ahmad
waqas.ahmad@aalto.fi

J. Helm
helmj@lafayette.edu

S. Bossuyt
sven.bossuyt@aalto.fi

P. Reu
plreu@sandia.gov

D. Turner
dzturne@sandia.gov

L.K. Luan
likang.luan@dantecdynamics.com

P. Lava
pascal.lava@matchid.eu

T. Siebert
tsiebert@lavision.de

M. Simonsen
simonsen@correlatedsolutions.com

¹ Department of Mechanical Engineering, Aalto University, Otakaari 4, Espoo 02150, Finland

² Department of Mechanical Engineering, Lafayette College, Acopian Engineering Center, Easton 18042, PS, USA

³ Sandia National Laboratory, Albuquerque, NM, USA

⁴ Dantec Dynamics, Kässbohrerstraße 18, 89077 Ulm, Germany

⁵ MatchID, Leikaai 25A, Gent B-9000, Belgium

⁶ LaVision, Anna-Vandenhoeck-Ring 19, Göttingen D-37081, Germany

⁷ Correlated Solutions, 121 Dutchman Blvd., Irmo, SC 29063, USA

Introduction

Digital Image Correlation (DIC) is a commercially available and commonly used non-contact, full-field displacement and strain measurement technique. Stereo-DIC provides improved flexibility over 2D-DIC by enabling the measurement of 3D shape and displacement [1]. In stereo-DIC, 2D correlated image points on two or more cameras are triangulated to reconstruct the 3D point position. Many commercial participants (hereafter referred as groups) sell a turnkey system that provides the hardware and software required for making stereo-DIC measurements.

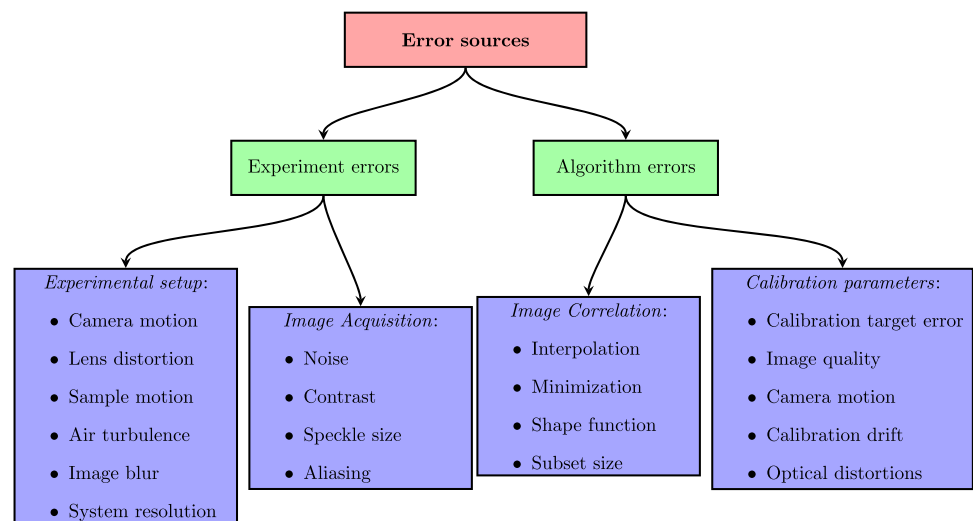
The International DIC Society (www.iDICs.org) organizes different challenges to provide a set of images that can help in verification and future development of the DIC codes in different applications [2, 3]. The “Stereo-DIC Challenge 1.0”, hosted by the iDICs, contributes to the development of stereo-DIC by providing a set of images from a well-controlled experimental setup for all codes to analyze. We benchmark five commercial codes against each other and to secondary measurement methods. This paper explains the details of the experiment and following analysis.

Many factors, listed in Fig. 1, contribute to the accuracy of DIC. These include quality of the speckle pattern [4–6], illumination conditions [7], size of image subsets used in the analysis [8, 9], calibration accuracy [10, 11], variation in temperature of the working environment [12] and correspondence of the points [13–15] etc.

While more work has been reported for quantification of 2D matching errors than 3D triangulated position errors [10], in this paper we study 3D stereo-reconstruction. A useful review of 3D reconstruction methods which are generally used in stereo-DIC is covered in [16]. The following journal

articles look at measurement uncertainty in stereo-DIC. Investigation of different stereo reconstruction methods on the accuracy of DIC has been reported using both simulations and experiments in [16]. In the study of the effects of bias on DIC, it was found that the interpolation function used in the cross-correlation results in a bias error in the 2D matching [17], which propagates to the 3D position. Additional noise bias was also reported in another study [18] which was further extended to analyze 3D error estimation to understand the theoretical effects of the calibration errors and 3D measurement uncertainty [14]. However, the derived equations for calibration measurement uncertainty were highly nonlinear and showed that an understanding of the variance and expectation of the calibration parameters did not easily propagate to 3D position uncertainty. Later, combination and propagation of the sensor and calibration uncertainties were also analyzed in [15] where nonlinear triangulation was used to calculate the uncertainty in position and strain in the world coordinate system. In order to find a simpler solution to the quantification of uncertainty in calibration, a Monte Carlo approach was reported in [13, 19, 20]. This method of measurement uncertainty was further extended by using a bootstrap Monte Carlo approach to correctly propagate the covariance of the calibration parameter errors based on methods in the Guide to Measurement Uncertainty published by Bureau International des Poids et Mesures (BIPM) [10]. To quantify the uncertainty of the measurements in stereo-DIC, comparison with benchmark physical experiments, involving translation and simple strains, has also been studied [21–23]. Although the input of these benchmarks confirms the general accuracy of the technique, most of these works do not provide details on the DIC experimental setup [10]. We seek to provide a common

Fig. 1 Major sources of error that contribute to the accuracy of DIC measurements



data set from a well-controlled experiment for the community to use in code development.

The main objective of the current stereo-DIC challenge was to provide a quality image set where the experimental error sources, other than the lens distortions, as mentioned in Fig. 1, were eliminated as much as possible. Lens distortions were both impossible to eliminate, but more significantly an important check on the calibration capabilities of the DIC software. To explore this both a wide-angle lens, with higher distortions and a moderate focal length lens, with lower distortions were used. This allowed the software errors to be studied from different stereo-DIC algorithms and to test their accuracy. Since the same image set was analyzed by all codes, the same experimental errors were present in all the results, hopefully simplifying the data interpretation. Any future development of stereo-DIC algorithms and accuracy can be tested using the same data set and analysis methods used in this paper. For this purpose, the Society for Experimental Mechanics (SEM) and the International DIC Society (iDICs) provide hosting for the stereo-DIC image sets. The calibration and translation files for the project can be freely accessed from: <https://idics.org/challenge/>. The image sets include both experimental and simulated images. We report in this paper only on the experimental image sets in detail. However, for completeness, the synthetic images are described in Appendix A.

All commercial, academic and research codes were invited to participate in the challenge via calls to participate at both the Society for Experimental Mechanics (SEM) and the annual iDICs conferences. The initial contact list contained 13 potential participants with existing Stereo-DIC codes. From this initial list, some codes were 2D implementations only, one commercial vendor chose to withdraw, and the remaining stereo codes did not submit results. Two global DIC codes were invited to participate but did not submit results. From the original 13 invitees, the following 5 groups submitted results that were analyzed in this paper: Dantec, LaVision, DICe, MatchID and Correlated Solutions. To maintain anonymity the results are presented as Group 1 through Group 5 in random order.

The paper includes the description of the experimental setup in Section 2, including the methods of capturing the data and the hardware used. Section 3 provides a description of the analysis methods used, which are implemented in a MATLAB code that is downloadable with the image sets. Results are provided in Section 4, with discussions and conclusions in Section 5.

Experimental Setup

The stereo-DIC image sets were acquired under carefully controlled experimental conditions to minimize all known DIC error sources. This included following all requirements

of the Good Practices Guide (GPG) as outlined in [1] when possible. Additional steps beyond the GPG included conducting the experiment on a large floating optical table in a climate-controlled room, with care taken to prevent heat waves from corrupting the results [24].

Stereo Sample

Figure 2 shows the dimensions of the DIC Challenge plate with features that include two triangular prisms with faces at 45° angles relative to the plate surface, two half cylinders with a radius of 0.25 inches (6.35 mm) in two different directions and a flat raised section with a height of 0.25 inches (6.35 mm). The sample was painted with a thin coat of white paint and speckled by hand using a Sharpie marker. Speckle sizes were large enough to ensure that they were not aliased, with average speckle size of 7.7 ± 1.5 pixels 32% coverage (Blob analysis) and 7.1 pixels (autocorrelation).

The as-built sample was measured with both a coordinate measuring machine (CMM) and laser scanned for comparison to the stereo-DIC results. For any future code validation, the surface maps are available with the images as a comma separated file with three columns of X, Y and Z. Dimensions are in mm. Appendix B Table 10 contains the laser scan specifications.

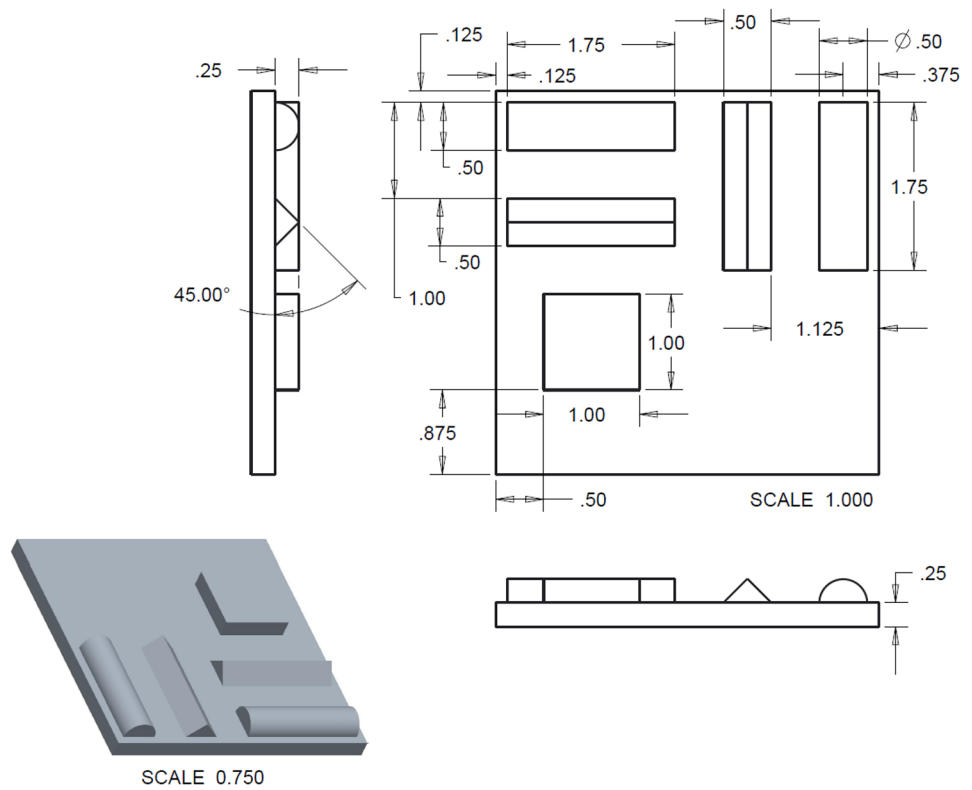
Stereo Camera Experimental Setup

The plate was mounted on a 2-axis Aerotech stage (ANT130-160-XY-Ultra) using a 90° angle plate. The setup from various views is shown in Fig. 3. The stage had a high-precision linear encoder and feedback control of the position (position accuracy better than ± 300 nm). The stage was setup to translate in the X and Z-directions from the view of the cameras. Total translation was ± 20 mm in both directions. Two stereo pairs were setup to view the plate. The 35 mm system used Edmund Optics lenses (DG Series) while the 16 mm system used Tamron lenses (Compact 5MP C-mount).

Figure 4 shows the lens distortions, without any corrections, of both lenses for a 50 mm in-plane translation. The lens distortion experiment was performed using a 101.6 mm (4 in) field-of-view (FOV) with camera plane perpendicular to the speckle patterned specimen. The distortion fields were obtained by translating the specimen in-plane along the two axes and removing the rigid body motion (RBM). The details of this method of measuring the lens distortion is described in [1]. The plot clearly shows that the distortion errors for the 16 mm lenses are 10× larger than for the 35 mm lens. The two lens focal lengths were chosen to test the lens distortion correction capabilities of the DIC calibration.

All four cameras were Point Grey (now Flir) Grasshopper 2 (Gras-50S5M) 5-Megapixel cameras with $3.45 \mu\text{m}$ pixels. As the 16 mm lenses required the cameras to be

Fig. 2 Designed dimensions of the translated plate. All units are in inches



closer to the plate (254 mm vs 600 mm standoff) to have the same FOV, they were positioned slightly above the mid-line of the sample looking down. The 35 mm cameras

were further back and positioned below the 16 mm setup to avoid heat waves from the front cameras, looking slightly up at the sample. The cameras were allowed to warm up

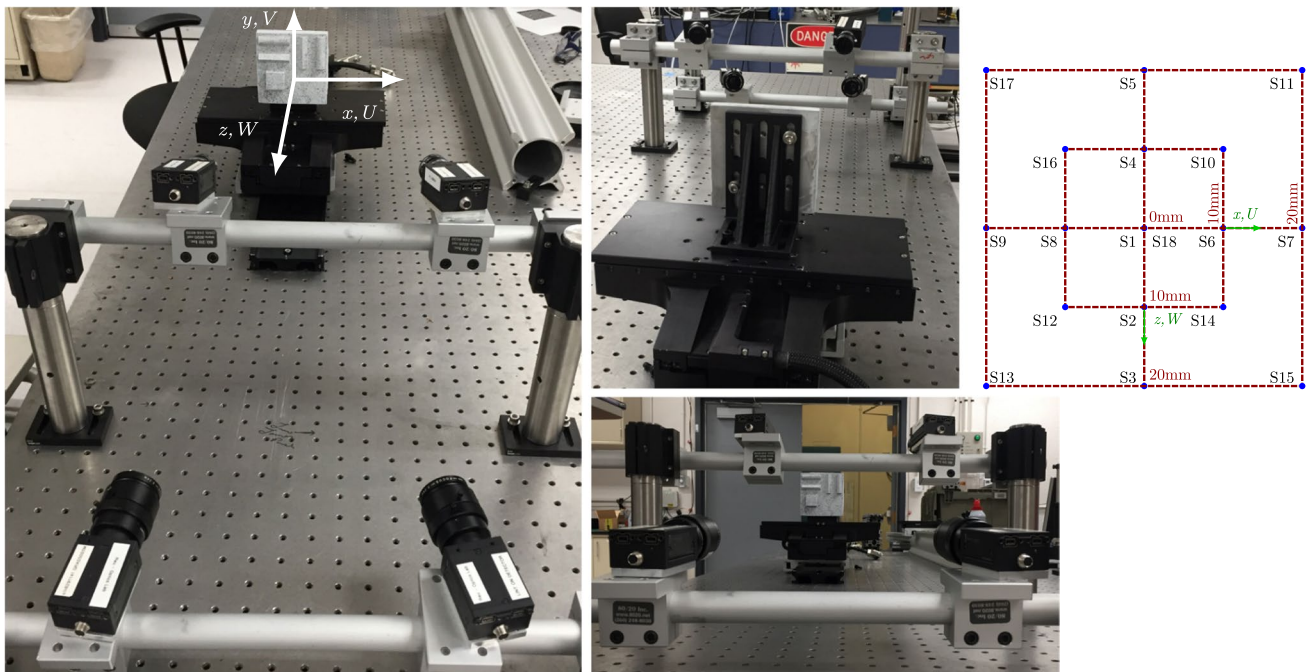


Fig. 3 Aerotech stage setup with the two DIC systems. 16 mm lenses closest to the sample and 35 mm lenses in the back. The DIC Coordinate system is shown in the left figure on the sample plate. Center two figures show a view from behind the sample and from directly behind the cameras. The plot on the right shows the top-down X and Z stage coordinate systems for the plate translation, distances moved and the corresponding Step number. Motion in the Y direction was not done due to the complexity of maintaining stage accuracy in that direction

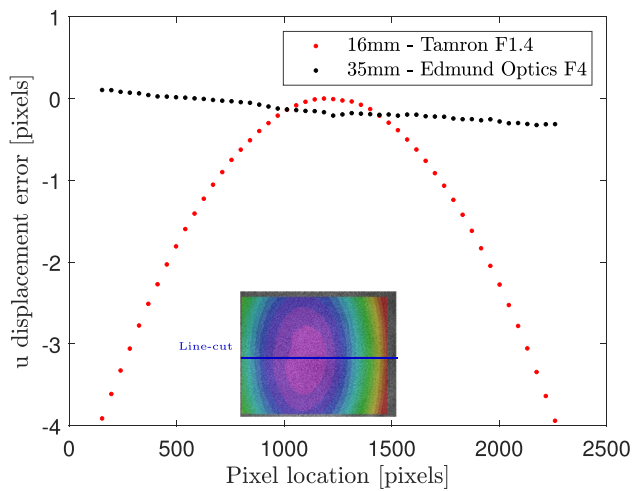


Fig. 4 Typical lens distortion error for the 16 mm Tamron lens and the 35 mm Edmund Optics Lens for a 50 pixel in-plane translation. Inset is the full-field distortion shape, with the plotted line-cut shown the inset line location. *Note:* The tilt in 35 mm lens plot is due to a misalignment between the camera and the plate

for an hour acquiring images before data was taken. Lighting was done with LED lights positioned a good distance away from the sample behind and above the cameras to minimize possible heat waves from the lights. Several images were captured prior to the experiment to evaluate noise and were also used to check for heat waves. Table 1 contains the experimental setup information.

Stereo Calibration Images

Stereo calibration images were captured using calibration targets provided by the groups for the specified field-of-view of the experiment. The calibration images are provided with the translation image sets. Table 2 shows the calibration

Table 1 Experimental parameters

Camera	Grasshopper 2 (Gras-50S5M)	
Image Size	2448x2048 pixels	
Aperture	≈ f/8	
Field-of-view	≈ 150 mm	
Focal Length	16 mm	35 mm
Image Scale	16.1 px/mm	16.6 px/mm
Stereo-Angle	19°	23°
Stand-off Distance	250 mm	600 mm
Image Acquisition Rate	≈ 0.5s/image non-uniform with a pause during stage translation	
Exposure Time	< 25 ms	
Patterning Technique	Hand Sharpie dots	
Pattern Feature Size	≈ 7 pixels	

targets used. The standard checkerboard calibration images (not shown in the table) were not taken experimentally, but rather were created using a stereo-DIC simulator [25] to provide as complete a set of calibration board types as possible. The dot grid calibration results were used to calculate the pin-hole camera intrinsic and extrinsic parameters to setup the simulator for creation of the checkerboard calibration images. Some calibration targets have both experimental and simulated images provided as noted in the table and Appendix A. The analysis in this paper used only the experimentally generated calibration images.

Translation Step Description

The plate was translated in the X- and Z-directions in steps of known amounts as shown in Fig. 3. Five images were taken at each position for calculating the noise or other averaging purposes. For the analysis presented here, Group 1 used the averaged image of the 5 images for DIC, while all other groups used the first image of each step. The field-of-view was set up to keep the sample in the image for all translated positions. The total experimental time to acquire images from Step 01 to Step 18 was approximately 8 minutes. Step 18 returned the stage back to the origin and serves as a measure of the system stability over the test period. The final step showed that the stage returned to within 10 nm of the original position as reported by the stage encoder. The DIC results also measured that it returned to the home position as indicated in the residual plots (Fig. 11 S18). Table 3 lists the step number, sample filenames, commanded stage displacement, and stage position standard deviation reported by the encoder.

Methodology

DIC Analysis

DIC analysis was conducted by the groups using their own software. No guidelines were given to the groups regarding the selection of regions-of-interest (ROI) other than to include as much of the sample as possible and include all the features. The ROIs could be either as a single large ROI, or as smaller ROIs on individual features. Other settings, including the subset size, interpolant or other parameters were left to the individual groups to decide. However, a step-size of 1 was required (i.e., a data point at every pixel that successfully correlated). Table 4 contains the DIC analysis parameters for each group [1]. Depending on the software package, some quantities may not be listed.

The data used for comparing the results was the X, Y and Z-Position in space, or the shape of the object at Step

Table 2 Calibration targets used to capture calibration images. Salient features of the targets along with the relevant vendors are also mentioned

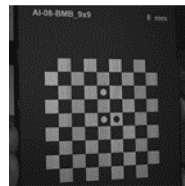
Calibration Board	Vendor
	Basic calibration target: 3 special dots Correlated Solutions, DICE and MatchID etc. 10 mm Dot Spacing Experimental & Simulated



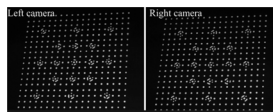
3D target with dots at 2 levels: LaVision (106-10) Experimental & Simulated



Checkerboard Calibration: Dantec 9×9-8mm Experimental & Simulated



Coded calibration targets: GOM/Trilion (CP20MV90x72) Experimental & Simulated



01 and the corresponding U , V , and W -Displacements at all following steps. The displacement magnitude A was calculated using:

$$A = \sqrt{U^2 + V^2 + W^2} \quad (1)$$

Strain was not calculated or analyzed for this paper.

Common Coordinate System for Transformation and Data Comparison

We used a model fit approach to compare the displacement results between different camera systems and the participating codes. For this, the Laser Scan data was used to fit a model to the measured shape of the object.

Specifications of the laser line probe are provided in the Appendix B. Figure 5(a) indicates the 8 surfaces scanned on the sample. They include the plate surface (Area 1), the mesa (Area 2), two 45° triangular prisms (Areas 3-6), and two 1/2-cylinders (Area 7,8). See Fig. 2 for the design drawing of the object and the dimensions.

We defined the model as the primitives of the object as they were oriented on the as-built part fit from the laser scan data. The CMM and DIC data both indicated that the as-built locations deviated from the drawing far enough that using the as-built laser scan data for fitting was required. Orientation of the submitted data was established by only fitting the data from the specimen features i.e., triangles, mesa and semi-cylinder as

Table 3 Position of each step, filename and standard deviation of the stage location

Step No.	Filename		W_{μ} (mm)	W_{σ} (nm)	U_{μ} (mm)	U_{σ} (nm)
	16mm Lens	35mm Lens				
01	Step01 00,00-sys1-0000_0.tif	Step01 00,00-sys2-0000_0.tif	0.000	6.755	0.000	7.014
02	Step02 00,-10-sys1-0000_0.tif	Step02 00,-10-sys2-0000_0.tif	10.000	6.160	-0.000	7.688
03	Step03 00,-20-sys1-0000_0.tif	Step03 00,-20-sys2-0000_0.tif	20.000	6.208	-0.000	6.304
04	Step04 00,10-sys1-0000_0.tif	Step04 00,10-sys2-0000_0.tif	-10.003	6.116	-0.000	7.673
05	Step05 00,20-sys1-0000_0.tif	Step05 00,20-sys2-0000_0.tif	-20.003	6.327	-0.000	6.745
06	Step06 10,00-sys1-0000_0.tif	Step06 10,00-sys2-0000_0.tif	-0.000	6.833	-10.007	4.908
07	Step07 20,00-sys1-0000_0.tif	Step07 20,00-sys2-0000_0.tif	-0.000	7.266	-20.007	5.713
08	Step08 -10,00-sys1-0000_0.tif	Step08 -10,00-sys2-0000_0.tif	-0.000	6.791	10.000	6.535
09	Step09 -20,00-sys1-0000_0.tif	Step09 -20,00-sys2-0000_0.tif	-0.000	7.371	19.999	5.690
10	Step10 10,10-sys1-0000_0.tif	Step10 10,10-sys2-0000_0.tif	-10.004	4.568	-10.007	5.992
11	Step11 20,20-sys1-0000_0.tif	Step11 20,20-sys2-0000_0.tif	-20.003	25.186	-20.007	14.654
12	Step12 -10,-10-sys1-0000_0.tif	Step12 -10,-10-sys2-0000_0.tif	10.000	6.429	9.999	7.645
13	Step13 -20,-20-sys1-0000_0.tif	Step13 -20,-20-sys2-0000_0.tif	20.000	6.537	19.999	6.102
14	Step14 10,-10-sys1-0000_0.tif	Step14 10,-10-sys2-0000_0.tif	10.000	6.076	-10.007	5.702
15	Step15 20,-20-sys1-0000_0.tif	Step15 20,-20-sys2-0000_0.tif	20.000	6.446	-20.007	5.136
16	Step16 -10,10-sys1-0000_0.tif	Step16 -10,10-sys2-0000_0.tif	-10.004	5.013	10.000	6.292
17	Step17 -20,20-sys1-0000_0.tif	Step17 -20,20-sys2-0000_0.tif	-20.003	6.072	19.999	5.988
18	Step18 00,00-sys1-0000_0.tif	Step18 00,00-sys2-0000_0.tif	0.000	7.587	-0.000	6.362

shown by blue areas in Fig. 5(b) and (c) (16 mm and 35 mm focal-length systems respectively). These points were designated by their pixel locations in Step 01, of the left camera for each lens focal length. The same areas were used for both systems to fit the model. The best-fit resulted in a common coordinate system for all the data. We then interpolated the data onto an x- and y-grid with spacing of 0.02 mm using MATLAB’s “ScatteredInterpolant”. This is a finer step than the DIC results, which were approximately 16 pixel/mm or 0.06 mm between data points. Any points with insufficient data density (neighbors) were removed. It is important to point out that while the discontinuous and transitional areas were

excluded during the coordinate system fitting, all the data on the plate that was submitted by the groups was interpolated into gridded data for comparison.

Stage Misorientation Correction

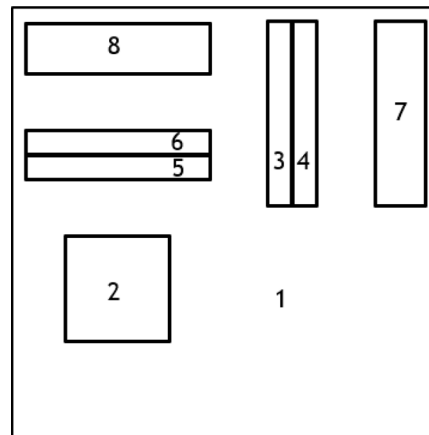
The mean values U , V , W and absolute displacements, measured by DIC, for each step were used to calculate a displacement error by subtracting these quantities from the motion of the translation stage. Initial comparison of the U , V and W error indicated a common bias error for all groups, while the *displacement error*, A , was similar. The common error strongly suggested a small misalignment of the coordinate

Table 4 DIC Analysis Parameters

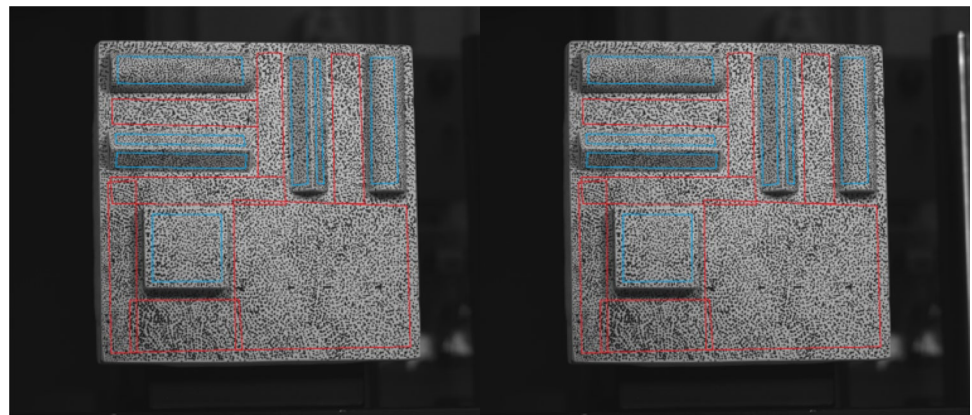
	Group 1	Group 2	Group 3	Group 4	Group 5
DIC Software	Latest version at the time of submission				
Image Filtering	Used Averaged images	None	None	None	None
Reference Image	Single reference image for each system	Single reference image for each system	Single reference image for each system	Single reference image for each system	Single reference image for each system
Interpolant	Keys 4 th Order interpolant	Bi-cubic spline	Bi-cubic spline	Bi-cubic spline	Optimized 8-tap spline
Matching Criterion	ZSSD	ZNSSD	ZNSSD	ZNSSD	NSSD
Subset Size	31	27	25	31	31
Step Size	1	1	1	1	1
Subset Shape Function	Affine	Bi-linear	Quadratic	Affine	Affine



Fig. 5 **a** (Top) Schematic of the plate. **b** Left camera image from 35 mm system and **c** 16 mm system. Enclosed areas in the red boxes, indicate image regions that were used for transformation into a common coordinate system. Blue regions were not used to fit the model but are included in the analysis



(a)



(b)

(c)

system of the translation stage and specimen surface. Figure 6 shows the rotation angles calculated to remove this bias error.

The angles α , β and γ were calculated by projection of the mean value of the U , V and W displacements for each step, on the known translation stage motion. From this, the average value of these angles was calculated using all steps. We then used the calculated average angles to transform the stage motion into the DIC coordinate system. Resulting vectors showed that the translation stage motion was not perfectly aligned with the stage motion, and therefore in the camera coordinate system not exactly 10 mm or 20 mm displacement. Misalignment corrected stage motion values are reported in Table 5. However, to simplify the plots, rounded even values were used for labeling in the plotted results but the corrected values are plotted.

Quality Metrics

The data submitted by the groups included differing numbers of data points since there were no guidelines provided about ROI selection. However, comparison using statistical parameters required a constant minimum ROI for all the

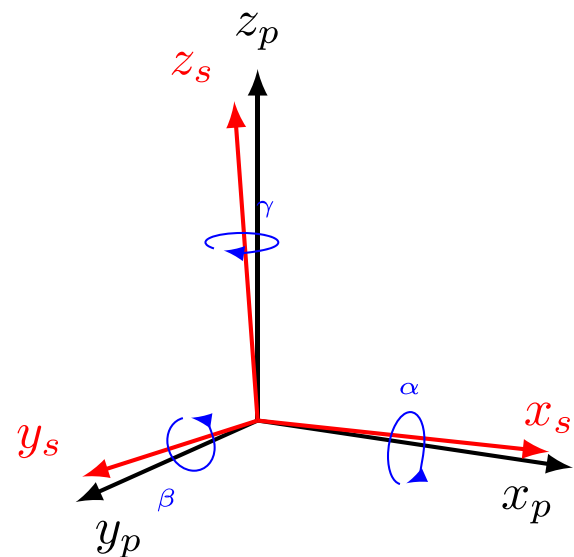


Fig. 6 x_s , y_s and z_s represent the coordinates of translation stage whereas x_p , y_p and z_p show the coordinates of the specimen. Alignment was done by transforming the stage coordinates system using the calculated misalignment angles: $\alpha = -0.0057^\circ$, $\beta = -0.5672^\circ$, $\gamma = -0.2406^\circ$

Table 5 Stage translation steps in the *U*, *V* and *W*-directions showing the uncorrected and the corrected translation amounts using the calculate misalignment

Step	U (mm)		V (mm)		W (mm)		A (mm)	
	Uncorrected	Corrected	Uncorrected	Corrected	Uncorrected	Corrected	Uncorrected	Corrected
1	0.000000	0.0000	0.0000	0.0000	0.0000	0.0000	0.0000	0.0000
2	0.000000	-0.0990	0.0000	0.0006	-10.0000	-9.9995	10.0000	10.0000
3	0.000000	-0.1980	0.0000	0.0012	-20.0000	-19.9990	20.0000	20.0000
4	0.000000	0.0990	0.0000	-0.0006	10.0000	9.9995	10.0000	10.0000
5	0.000000	0.1980	0.0000	-0.0012	20.0000	19.9990	20.0000	20.0000
6	10.000000	9.9994	0.0000	0.0420	0.0000	-0.0990	10.0000	10.0000
7	20.000000	19.9988	0.0000	0.0840	0.0000	-0.1980	20.0000	20.0000
8	-10.000000	-9.9994	0.0000	-0.0420	0.0000	0.0990	10.0000	10.0000
9	-20.000000	-19.9988	0.0000	-0.0840	0.0000	0.1980	20.0000	20.0000
10	10.000000	10.0984	0.0000	0.0414	10.0000	9.9005	14.1421	14.1421
11	20.000000	20.1968	0.0000	0.0828	20.0000	19.8010	28.2843	28.2843
12	-10.000000	-10.0984	0.0000	-0.0414	-10.0000	-9.9005	14.1421	14.1421
13	-20.000000	-20.1968	0.0000	-0.0828	-20.0000	-19.8010	28.2843	28.2843
14	10.000000	9.9004	0.0000	0.0426	-10.0000	-10.0985	14.1421	14.1421
15	20.000000	19.8008	0.0000	0.0852	-20.0000	-20.1970	28.2843	28.2843
16	-10.000000	-9.9004	0.0000	-0.0426	10.0000	10.0985	14.1421	14.1421
17	-20.000000	-19.8008	0.0000	-0.0852	20.0000	20.1970	28.2843	28.2843
18	0.000000	0.0000	0.0000	0.0000	0.0000	0.0000	0.0000	0.0000

submissions. Therefore, only areas that are captured by all the participants have been included for analysis. However, because coverage of the sample is important, a second scoring system was devised to indicate the coverage of the measurement area.

After transforming the displacement data for each step and each group as described earlier, and interpolating onto a common grid for the data, the following quality metrics were calculated.

1. Measurement of the mesa height, angle and heights of the triangles and radius of the cylinders. These measured values were compared with the laser scan measurements. For this, laser scan data was also transformed into a common coordinate system. A line-cut was taken to include the transformed data from a mesa, triangle and cylinder as shown in Fig. 7.
2. DIC Coverage, i.e., how close to edges and the peak of the triangle the codes were able to calculate. The scoring system for the coverage area was based on:
 - how close to the critical edges the data was analyzed and,
 - how much of the area of the specimen was analyzed by each group.

To check the missing data around the edges of the mesa, triangles, and cylinders, a binary mask was created from the edges of the plate and the features on the

plate using the laser scan data. Euclidean distance in the 2D-plane of every pixel in the ROI was calculated based on the nearest edge in the binary mask. Only pixel locations with missing data were used to find the score of each group using a root mean square (RMS) of the

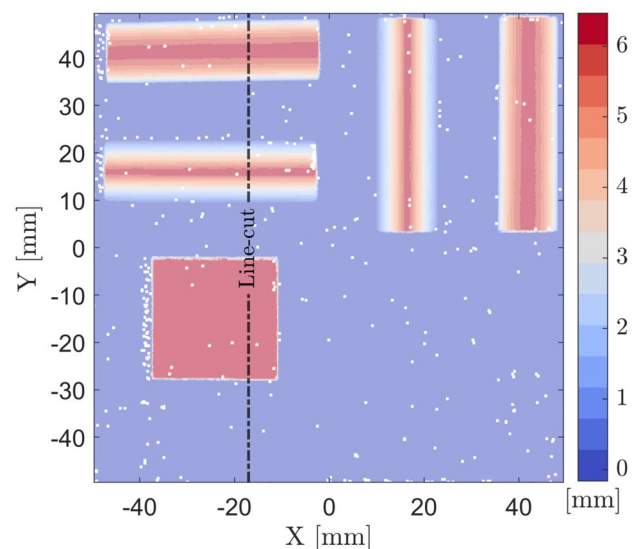


Fig. 7 Laser scanner data transformed to the DIC common coordinate system. Units are in mm. Dotted line shows the line-cut that was used to extract the feature height data from the DIC and laser scan. The features included the mesa, a triangle, and a cylinder

Euclidean distance. To compare the overall coverage by each group, percentage coverage was calculated by dividing the number of pixel locations with data to the total number of possible data points on the plate.

3. Measured DIC translation distance which was calculated from the mean displacement at a particular step. This value was compared to the known corrected stage translation. Residual fields were obtained after subtracting the mean value of each step for every group. Comparison of the residual fields, between the groups, was done using the absolute displacement, A , which was calculated by using equation (1). Nonetheless, the individual displacement components U , V and W plots are available as supplementary material at <https://aaltodoc.aalto.fi/handle/123456789/120731>.

Results

We compared both the measured sample shape and the displacements between the DIC results and a secondary measurement. The results for the shape measurement are discussed in Section 4.1, the DIC coverage is discussed in Section 4.2, the displacement magnitude results are presented in Section 4.3, and the individual U , V and W displacement results in Section 4.4.

3D Shape Measurement Comparison to the Laser Scan

The 3D shape of the sample was compared between the DIC shape and the laser scan data using the line-cut shown in Fig. 7. Figure 8(a) plots the results of the Z-height along the Y-axis for all 5 groups for the 16 mm system. The 35 mm results are not shown as they appear identical at this scale. Because the scale makes it difficult to compare, the difference between the laser and DIC is also calculated using:

$$\Delta Z = Z_{\text{DIC}} - Z_{\text{laser}} \quad (2)$$

ΔZ is plotted in Fig. 8(b) for the 35 mm system and Fig. 8(c) for the 16 mm system. All 3 figures are aligned to illustrate the issues at the edges of each of the shapes. Blue dashed lines in the figure highlight the edge of the mesa and the peak of the triangle. Also of note, is the bias error across the cylinder. Fig. 8 also illustrates the impact of selecting the ROI for the analysis. Group 4 clearly had results closer to the edges of all the features, but with the impact of larger errors at those locations. For all codes over the flat regions, the errors are less than $33\mu\text{m}$. The jagged appearance of the line is caused primarily by noise in the laser scan data. The noise is illustrated as an inset in Fig. 8(a) showing a zoomed in section from the flat portion of the plate that shows the laser scan noise relative to the smoother DIC results. The triangle region showed errors between $50\mu\text{m}$ and $100\mu\text{m}$.

Figure 8(b) and (c) indicate that error on the left face of the triangle was larger as compared to the right face. It was also observed that any data lost during the analysis of different steps would have missing data on the same left face. The left face errors were larger because of the perspective view from the right camera deforms that face more and creates larger errors during the cross-correlation. Group 4 dropped a significant amount of data from left face of the triangle at Step 17, whereas similar error values were observed for the right face from all the groups in both 35mm and 16mm lens system. Moreover, error values increased for the 16mm lens on both the cylinder and the top edge of the triangle however, the scale of the error was similar to the 35mm lens system on the mesa.

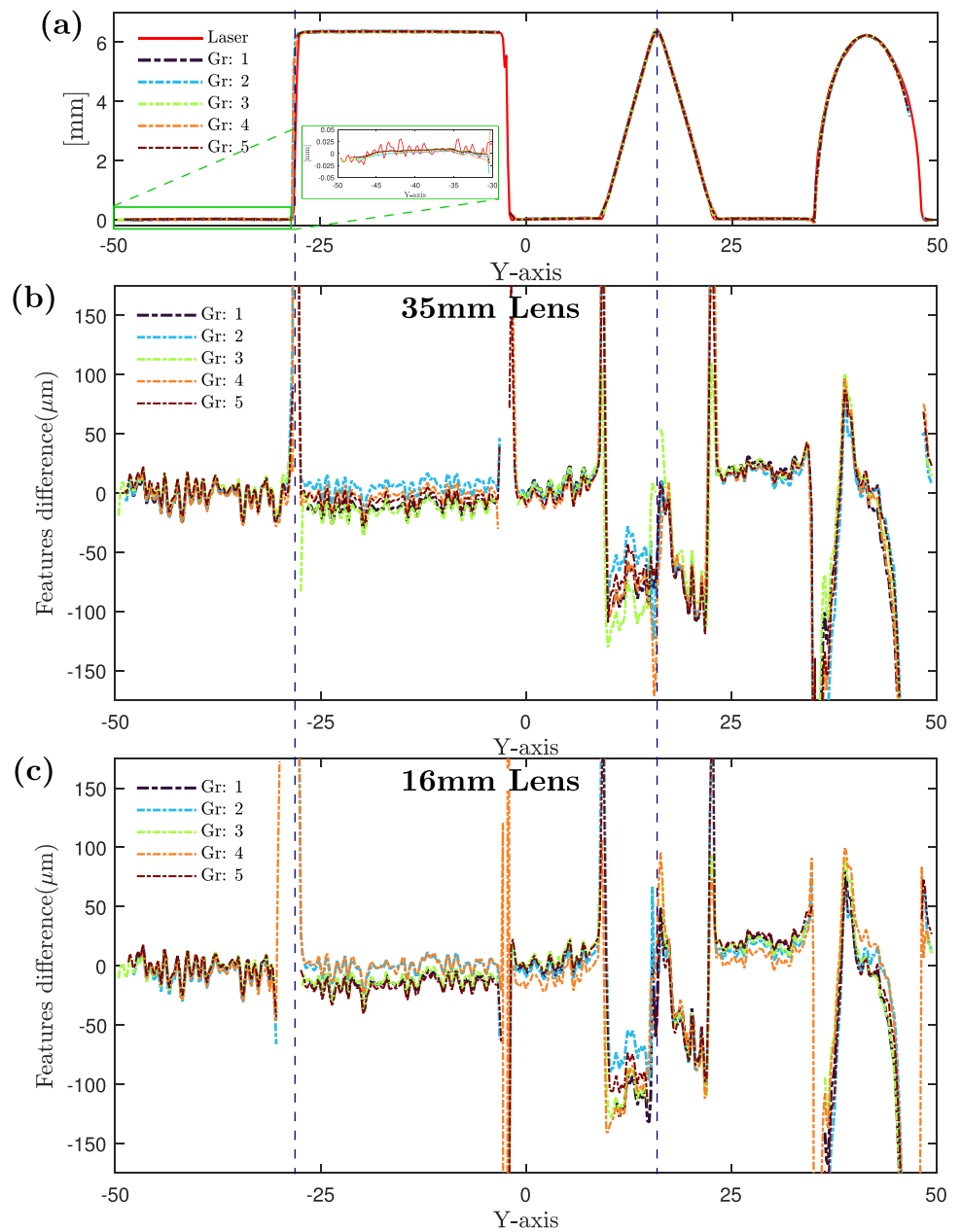
DIC Coverage of the Sample

The results presented for the displacement errors in the following sections used data only where *all* codes had results. The displacement error highlighted that not all codes calculated data everywhere on the sample. Missing data is expected, as DIC cannot handle discontinuities, such as at the triangle peak and edges, cylinder edges, and mesa edges, and any region that is not visible due to the view angle¹. Some codes restricted the ROI to exclude those known problem areas, while others correlated over that region. This is illustrated in Fig. 9 which shows the Euclidean XY-distance of the pixel locations with missing data. The smaller the number, the lower the distance, and the closer to the edge the data was obtained. However, there were other regions where data was missing from different groups depending on different quality metrics in the DIC code such as epipolar constraints or some other matching quality. Missing data was more pronounced on the cylinder locations at the extreme corners of the displacement and on the peak of triangle as shown in Fig. 9.

Table 6 data show that the maximum amount of data was discarded at step 17 (top left corner motion of stage) for most of the groups indicated by the maximum RMS value at this step. The minimum RMS value was recorded for Group 2 at Step 15 in which the specimen was moved to bottom right corner. Lastly, higher RMS scores were observed for the 16mm lens system when compared to the 35mm lens system, which means that more data was dropped around the critical edges for the 16mm system.

¹ In the current stereo-DIC challenge specimen, a region around the mesa was not visible in one of the cameras due to stereo-occlusion and was dropped during correlation. However, during the coverage score, these points were considered as missing data thus, effected the RMS score of each group equally.

Fig. 8 Vertical line cut with the bottom of the specimen on the left and the top on the right. Measurement of step height, angle and heights of the triangles, and the radius of the cylinders at the line-cut location drawn in Fig. 7: **a** comparison of the DIC data with laser scan data for 16mm lens system, **b** error between the DIC measurements and laser scan for the 35mm lens system and **c** for the 16mm lens systems



Absolute Displacement Magnitude Residuals

Residual fields (A_{Res}) for all the groups were calculated by subtracting the value of the stage displacement (A_{Stage}) from the measured DIC results (A_{DIC}), calculated from all the points in the ROI common to all groups.

$$A_{Res} = A_{DIC} - A_{Stage} \quad (3)$$

Results for the 16mm lens system are shown in Fig. 10 and for the 35mm lens system in Fig. 11. All group results are shown individually in the Appendix C (Figs. 19,

20, 21, 22, 23, 24, 25, 26, 27 and 28). An example of residual full-field plots, of the absolute displacement, with respect to the motion of the plate are shown in Fig. 10(a) and 11(a). The difference between the mean DIC value of each step and the actual rigid body motion of the translation have also been plotted along with the standard deviation for each step in a radar plot in Figs. 10(b, c) and 11(b, c). The labels (S1-S18) in the radar plots were chosen such that two steps, that had opposite translation compared to origin steps, were plotted on same line of the radar plot. For example, step S2 represents a motion of (0, -10mm)

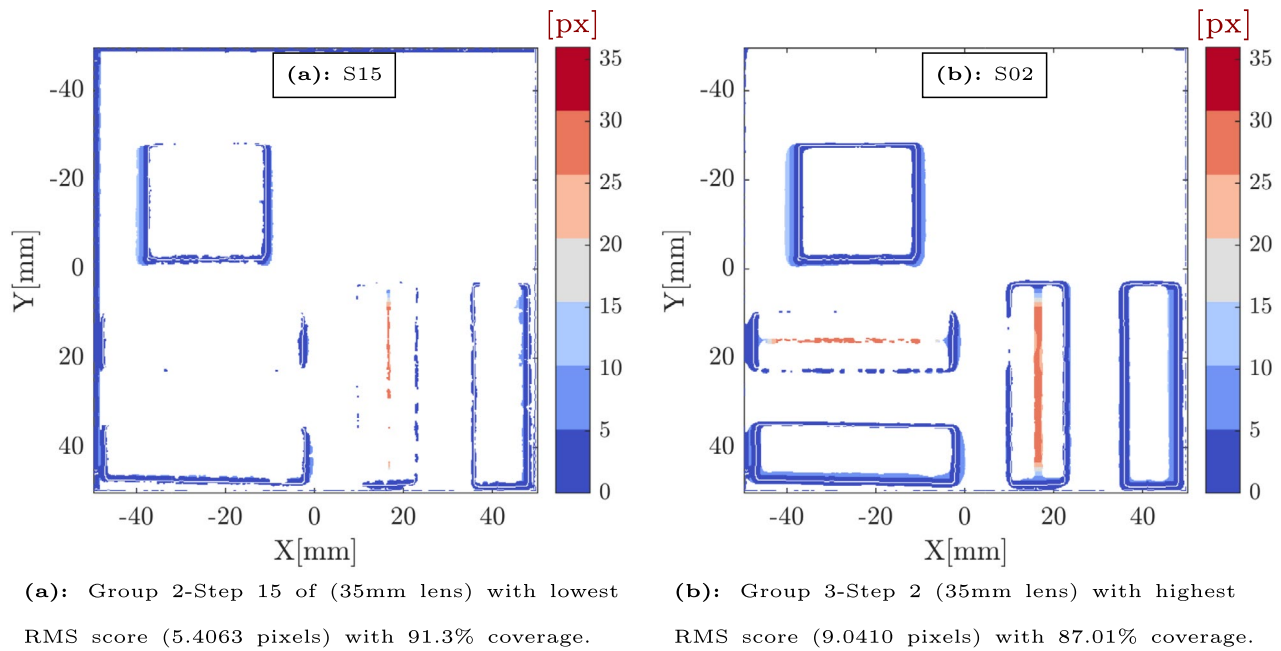


Fig. 9 Euclidean distance map of the missing ROI for 35mm lens system: **a** Step 15 for Group 2, the code with the closest coverage around the critical edges **b** Step 2 for Group 3, the code with the highest RMS value due to missing data on the triangle peaks. *Note:* colorbar in pixels

while S4 moved (0, 10mm). Therefore, error values of these steps were shown on the same line in the radar plots. The colorbar limits have been set individually for each group and aids in interpreting the residual field plots for any individual group. Residual fields for each step were also analyzed with fixed colorbar limits for each step for all groups to aid in

comparison between groups. These results are available as supplementary material.

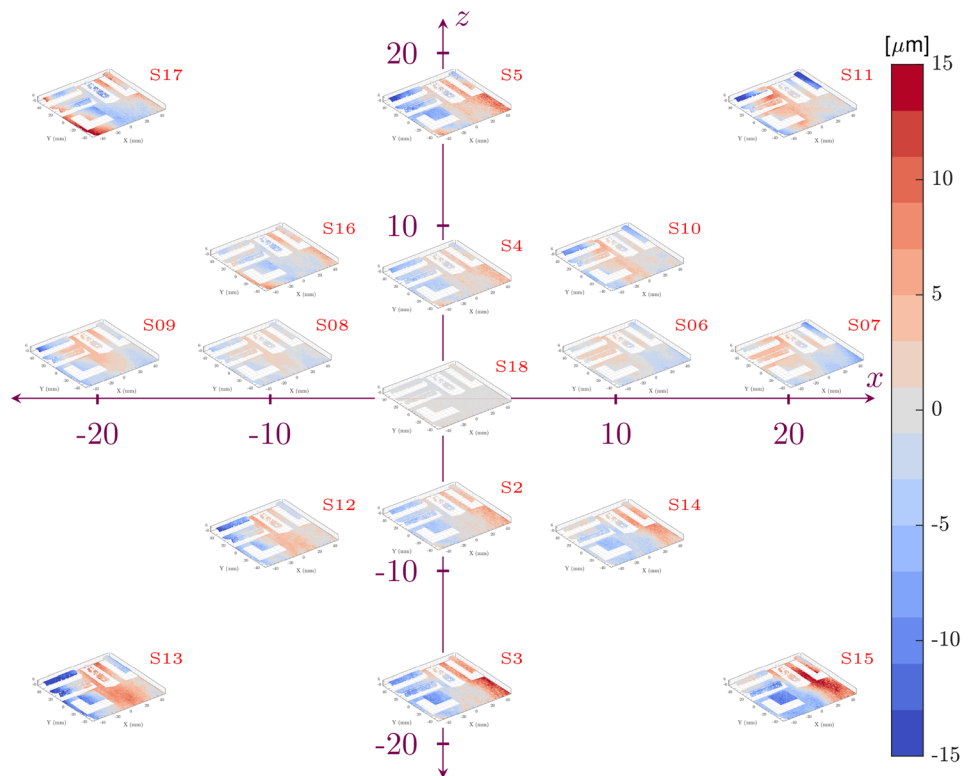
An important advantage of using the displacement magnitude is that misalignment errors, as discussed earlier, are not important. The figures reveal that Group 2 consistently underestimated the mean displacements for both lens

Table 6 (Left) Minimum and maximum root mean square errors of the Euclidean distance map for each group indicating which step had the most missing data (higher RMS) or least missing data (Lower RMS). (Right) Percent coverage of the sample comparing the number

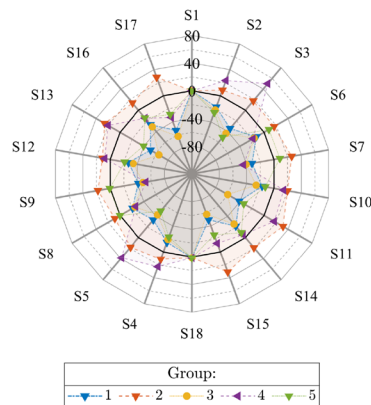
of data points measured with the maximum possible number of data points. 100% coverage is not expected¹, although a higher percentage indicates more coverage

Gr:	Root mean square Euclidean distance				Percentage coverage			
	Minimum RMS		Maximum RMS		Minimum Coverage		Maximum Coverage	
	35mm Lens	16mm Lens	35mm Lens	16mm Lens	35mm Lens	16mm Lens	35mm Lens	16mm Lens
1	7.4709 (Step 01)	8.6456 (Step 01)	7.4709 (Step 01)	8.6550 (Step 01)	75.24 (Step 01)	72.94 (Step 01)	75.24 (Step 01)	73.05 (Step 01)
2	5.4063 (Step 15)	8.2691 (Step 03)	5.4293 (Step 09)	8.7578 (Step 17)	91.27 (Step 17)	86.02 (Step 11)	91.35 (Step 01)	86.56 (Step 01)
3	8.6293 (Step 01)	9.6482 (Step 01)	9.0410 (Step 02)	10.1353 (Step 17)	87.01 (Step 02)	83.40 (Step 17)	89.94 (Step 01)	87.02 (Step 01)
4	6.5613 (Step 15)	6.3337 (Step 18)	6.9848 (Step 17)	7.2729 (Step 17)	88.38 (Step 17)	86.67 (Step 17)	88.99 (Step 01)	88.37 (Step 01)
5	5.667 (Step 16)	7.8332 (Step 01)	5.8356 (Step 17)	8.5502 (Step 17)	91.32 (Step 17)	86.91 (Step 17)	91.39 (Step 01)	88.15 (Step 01)

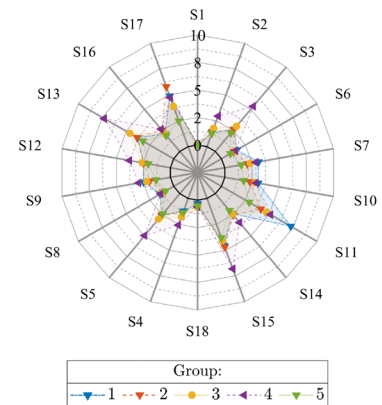
Fig. 10 16 mm Lens, Absolute displacement. **a** Residual plots of the A_{Res} for the entire ROI at all steps. Axis values indicate the displacement in mm. Colorbar scale is in μm . **b** Mean, μ , of the ROI at each step. **c** Standard deviation, σ , of the ROI at each step. The radial scale is in μm



(a) Residual fields of A at each step.



(b) $\mu(A_{stage} - A_{DIC})$



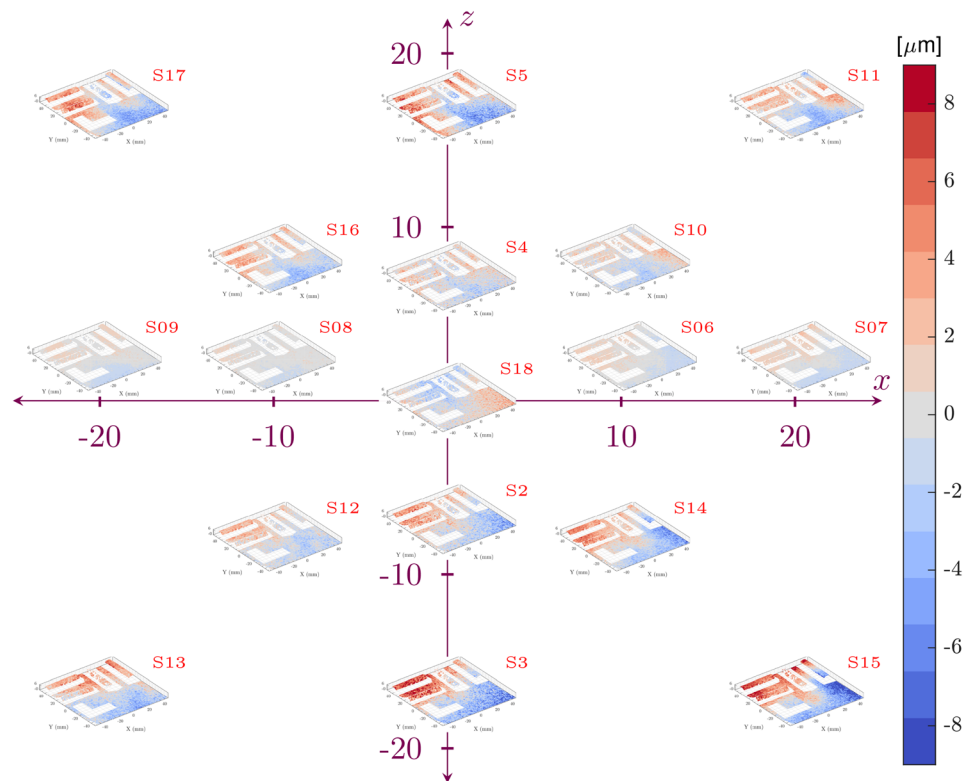
(c) $\sigma(A_{DIC})$

systems compared to other groups which overestimated the value of displacement (see mean radar plot). For the 16mm lens, Group 4 underestimated the extreme steps motion normal to camera baseline (Step 3 and Step 5) while overestimated the motion at the corner of the baseline i.e., Step 7 and Step 9. Group 5 gave the smallest error for the 35mm lens compared to other codes. However, for the 16mm lens, its error was greater compared to other groups. With a few

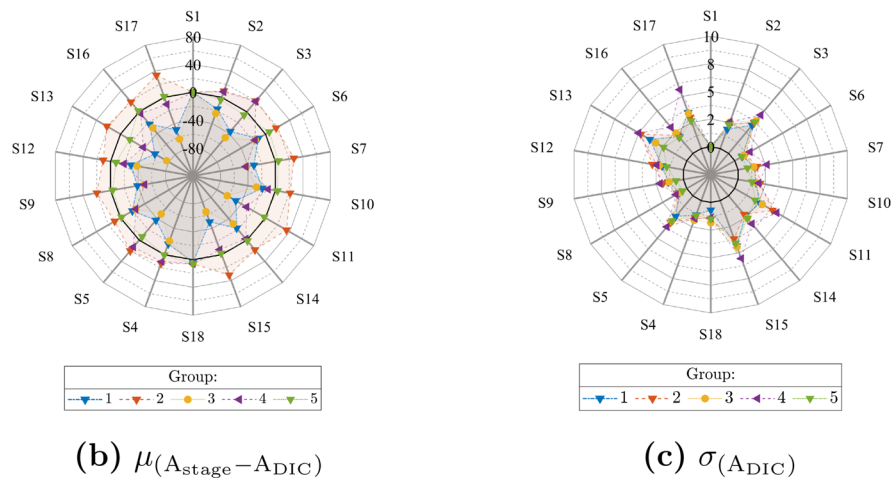
exceptions mentioned earlier, all the groups overestimated the error when the plate motion was orthogonal to the camera baseline for the 16mm lens.

It is interesting to also compare the results at an extreme corner of the data set. Table 7 shows the absolute displacement residuals plot at Step 17, the top-left corner of the displacement (using the corrected data). In this case some codes better correct for the distortions at this extreme location. Earlier

Fig. 11 35 mm Lens, Absolute displacement. **a** Residual plots of the A_{Res} for the entire ROI at all steps. Axis values indicate the displacement in mm. Colorbar scale is in μm . **b** Mean, μ , of the ROI at each step. **c** Standard deviation, σ , of the ROI at each step. The radial scale is in μm



(a) Residual fields of A at each step.



(b) $\mu(A_{\text{stage}} - A_{\text{DIC}})$

(c) $\sigma(A_{\text{DIC}})$

observations and Table 7 show that results depended on how effectively different codes were able to account for distortions at the extreme ends especially for the case of the 16 mm lens.

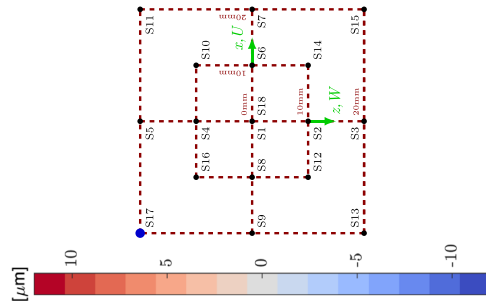
Comparison of the U, V and W Displacements With the Stage Translations

Figure 12(a–c) shows the results for all 5 groups for the U , V , and W -displacements before the final correction for the 16 mm lens (35 mm lens had similar results). An offset can be seen in the results by corresponding the step number with

the bias. Using this information, the plate misorientation can be calculated as discussed in Section 3.3. After final alignment of the DIC coordinate system with the plate, the U , V , and W -displacements can be compared to the corrected commanded stage translation. Figure 12(d–f) show the results after correcting the misalignment, showing that the bias errors have been removed. The correction is most clearly seen in the V -displacement Fig. 12(b, e) where the displacement residual is now uniform for all positions.

$$U_{\text{RES}} = U_{\text{DIC}} - U_{\text{StageCorr}} \quad (4)$$

Table 7 (Step : 17) A Displacement: Error map for each group with translation stage motion shown with blue dot on the grid. Abbreviation μ is used to denote mean value of displacements i.e., U_{DIC} , V_{DIC} , W_{DIC} , and A_{DIC} , subtracted from the corrected translation stage motion. Whereas σ denotes the standard deviation calculated from the AOI for a particular displacement field, U_{DIC} , V_{DIC} , W_{DIC} , and A_{DIC} . ΔA shows the residual field after removing the mean displacement calculated from DIC. Resulting error reported in $A_{(\mu\pm\sigma)}$ columns. *NOTE:* All units in μm



Group	$U_{(\mu\pm\sigma)}$	$V_{(\mu\pm\sigma)}$	$W_{(\mu\pm\sigma)}$	$A_{(\mu\pm\sigma)}$	35mm lens (ΔA)	16mm lens (ΔA)
1 (35mm)	35.51 ± 1.85	12.24 ± 2.15	-34.56 ± 3.47	-49.57 ± 3.45		
1 (16mm)	43.99 ± 3	18.69 ± 1.78	-31.36 ± 7.96	-53.24 ± 4.89		
2 (35mm)	-24.45 ± 2.58	11.98 ± 1.98	23.07 ± 3.25	33.56 ± 2.98		
2 (16mm)	-19.65 ± 2.01	16.77 ± 1.92	20.53 ± 8.35	28.37 ± 5.8		
3 (35mm)	45.42 ± 1.68	-31.97 ± 1.11	-44.83 ± 3.58	-63.69 ± 3.36		
3 (16mm)	45.86 ± 2.19	-53.27 ± 2.12	-42.51 ± 5.31	-62.25 ± 3.89		
4 (35mm)	35.39 ± 4.19	7.84 ± 7.58	19.7 ± 8.4	-10.7 ± 5.65		
4 (16mm)	89.89 ± 8.62	27.01 ± 10.99	41.53 ± 12.12	-33.18 ± 4.73		
5 (35mm)	-4.22 ± 1.15	7.9 ± 1.23	-2.56 ± 2.84	1.1 ± 2.67		
5 (16mm)	-9.47 ± 1.52	-5.11 ± 1.51	-49.36 ± 3.46	-28.57 ± 2.49		

$$V_{RES} = V_{DIC} - V_{StageCorr} \tag{5}$$

$$W_{RES} = W_{DIC} - W_{StageCorr} \tag{6}$$

Figure 13 shows the same corrected displacement residuals for both the 16 mm and 35 mm lenses. Note that the scales have been changed from Fig. 12. Corresponding to the mean error at each stop, the standard deviation was also calculated and is plotted in Fig. 14 for both lens systems. The standard deviation of the full-field residual is larger for the 16 mm lens (Fig. 14(d–f)) when compared to the 35 mm lens (Fig. 14(a–c)). The larger error is most likely due to uncorrected lens distortions and is most pronounced in Group 4.

Full-Field Error Discussion

One notable difference in the full-field results was a moiré-like pattern seen in the V-displacement for Group 2. Figure 15 shows two full-field results from Step 17 for the 35 mm lens. Group 2 shows clear moiré-like banding at all steps. The banding is most pronounced in the V-displacement but is also visible in the U and W as well. These were attributed to the systematic error due to the implementation of triangulation in the software. A comparison with other groups highlighted this issue and was resolved in the code. Group 1 submitted some results that also showed the banding, but ultimately used an averaged image (or results) from the 5 images taken, and the banding was removed. The averaged results were used because too much data was dropped from the results that used only one image due to other software settings.

Pattern induced bias (PIB) is also evident in the results as the mottled pattern seen in the images in Fig. 16. PIB results from the interaction of the non-uniform pattern within a subset and the undermatched shape function of the subset biasing the results in one direction, creating a fixed bias error spatially. The PIB error is unrelated to the image noise, but purely due to the minimization being biased by the underlying image gradients. Figure 16 shows PIB error in both the U and W displacement field for Group 1. The error seen is almost certainly PIB as the images were averaged before correlation reducing/eliminating any image noise that could cause errors in the matching.

Also note the large amount of missing data on the left face of the vertical triangle. The missing data is caused by camera software setting that removes questionable data. Figure 17 shows the two camera views (cropped to the size of the test piece) illustrating the large perspective shift. No data was lost for this particular code.

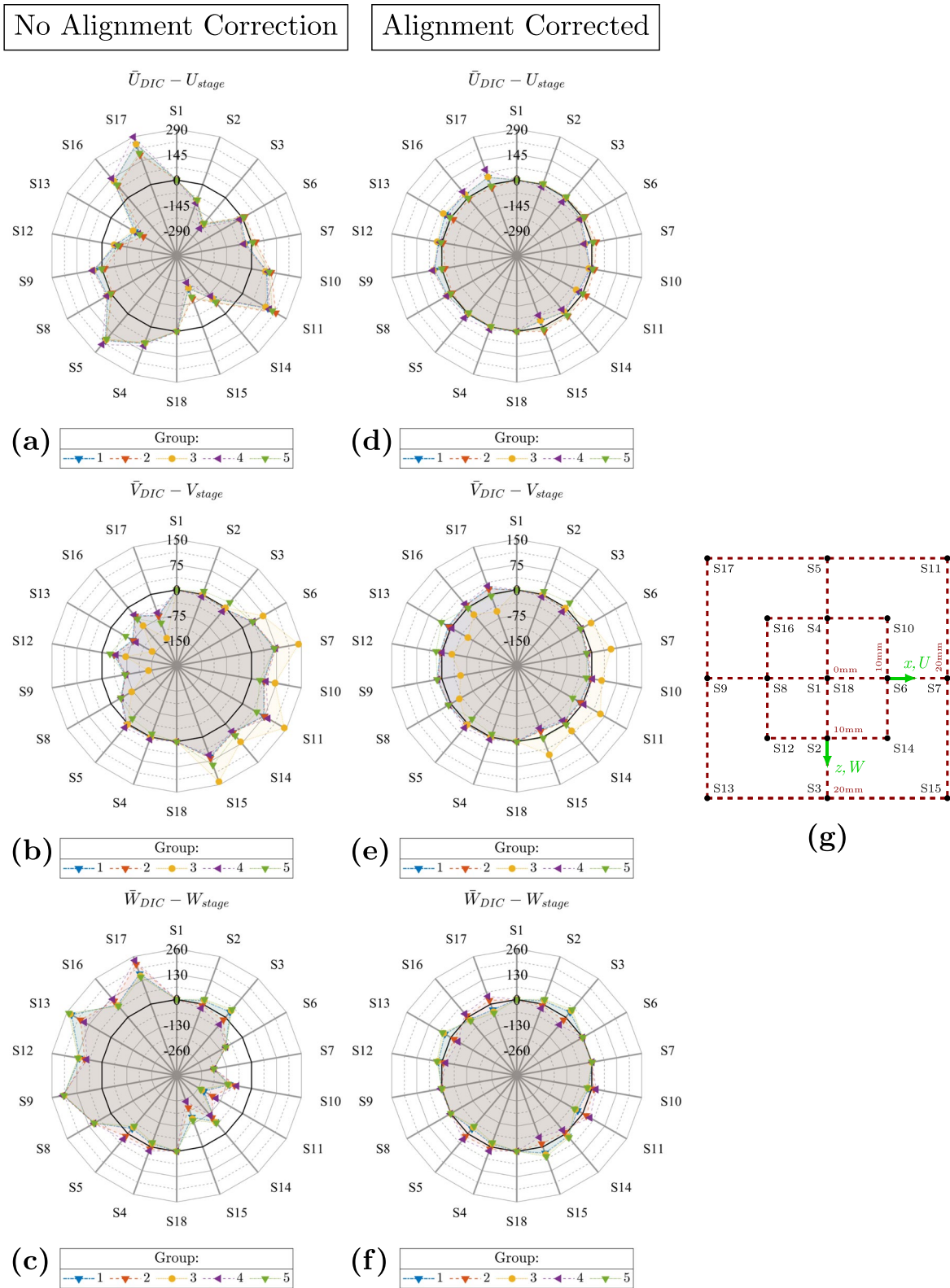


Fig. 12 All displacements in μm . **a**, **b** and **c** Show the error for the mean of U, V and W without misalignment correction while **d**, **e** and **f** show results after misalignment correction for 16 mm lens system. **g** Stage numbering and the stage displacement at each step

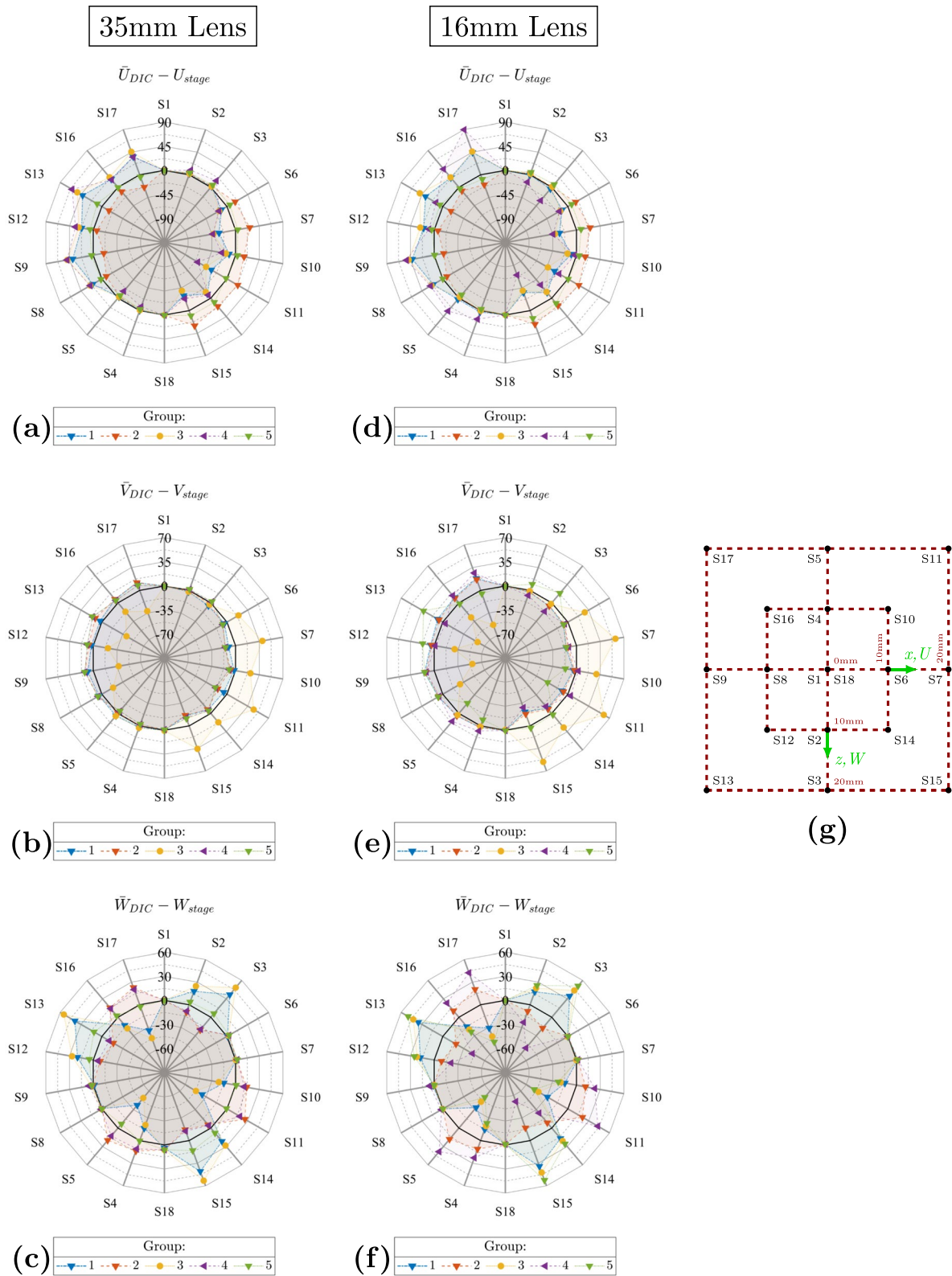


Fig. 13 All displacements in μm . **a, b, c** Displacement residuals for the 35 mm system. **d, e, f** Displacement residuals for the 16 mm system. **g** Stage numbering and the stage displacement at each step

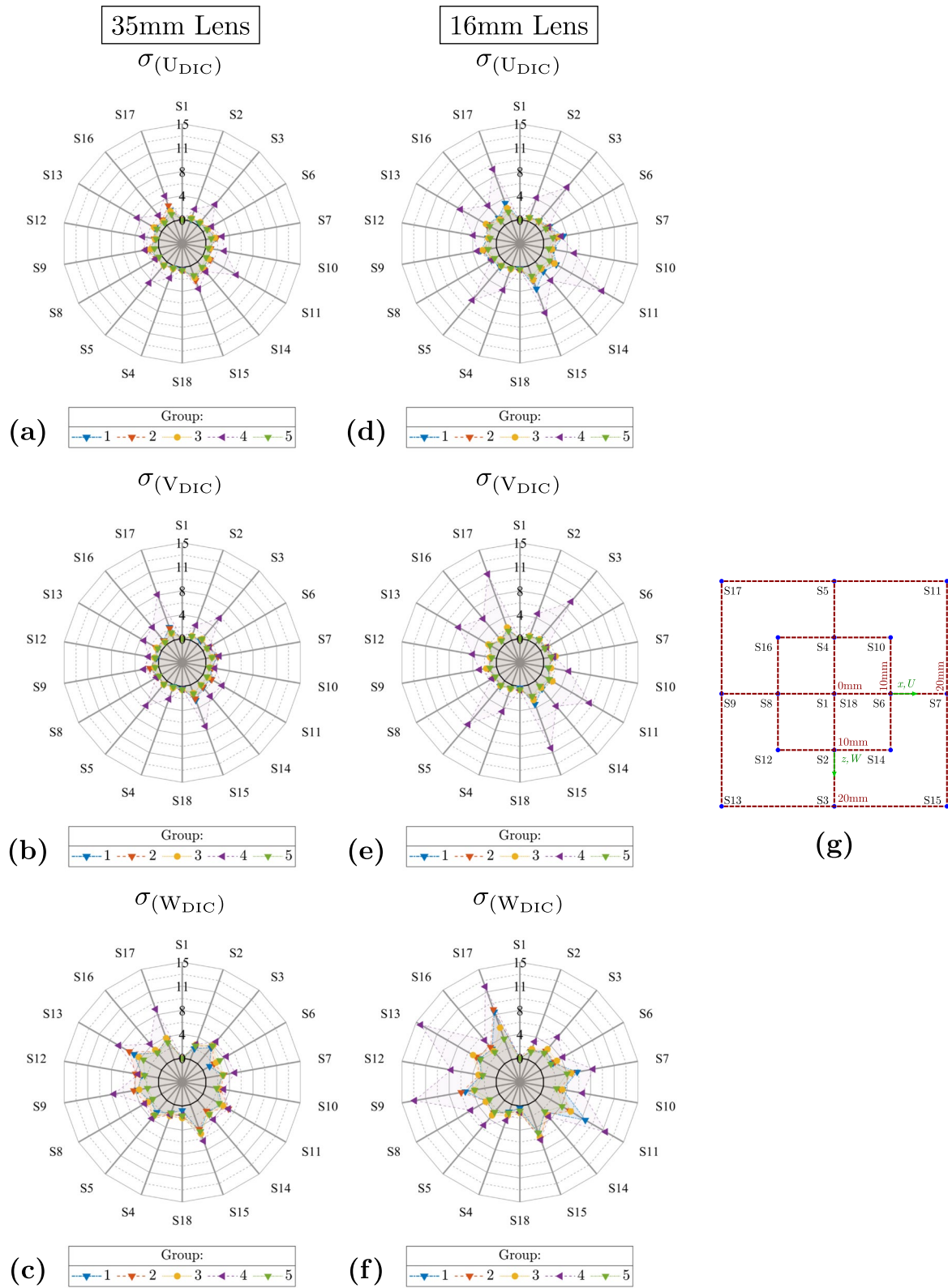


Fig. 14 All displacements in μm . **a, b, c** Standard Deviation of the displacement residuals for the 35 mm system. **d, e, f** Displacement residuals for the 16 mm system. **g** Stage numbering and the stage displacement at each step

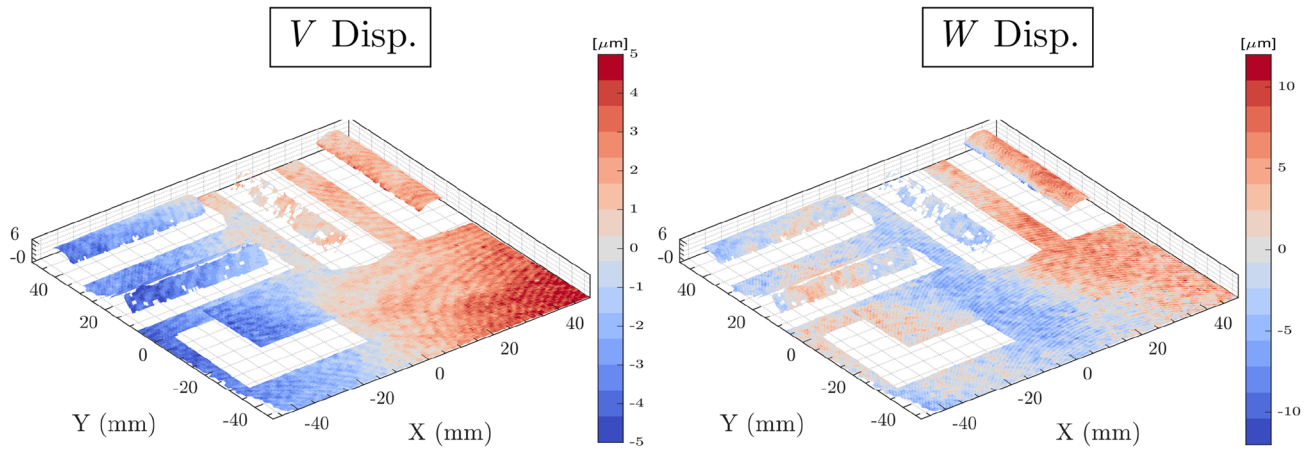


Fig. 15 Moiré effect shown in the V-displacement (left) and W-displacement (right) field for Group 2 and 35 mm lens

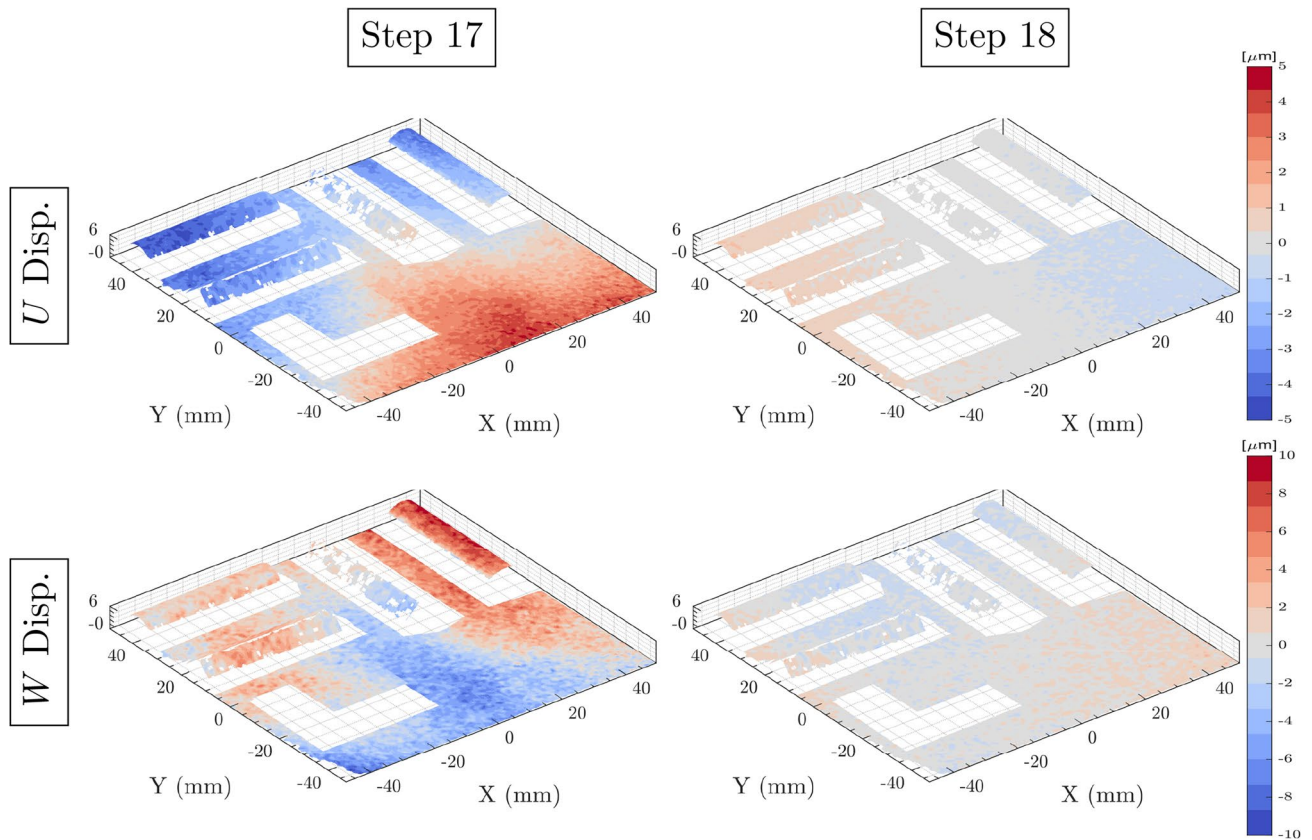


Fig. 16 PIB error shown in the U-displacement (Top) W-displacement (Bottom) for Step 17 (left) and Step 18 (right) for Group 1 and 35 mm lens

Table 8 shows the maximum error comparison between different participants for both lens systems. The step at which maximum error was recorded is noted in the table for each displacement field along with the corresponding residual plots of absolute displacements shown in the last two columns. Table 8 shows that Step 13 and Step 15 motion, at the bottom extremes, resulted in the maximum U error for all the groups for the 35 mm lens system. However, for the 16 mm lens, Group 1 and Group 4 recorded maximum error for Step 17 (top left corner). Whereas for V displacement, Step 11 and Step 15 recorded the maximum errors. Error values of

Group 3 were maximum in V displacement compared to other groups. Lastly, for W displacements, bottom right motion (Step 15) and top right motion (Step 11) gave maximum error values with highest recorded value from Group 5. Comparing the error values between different groups in terms of U , V and W suggests that extreme motions on the right caused maximum error. However, if we take the magnitude of the displacements, which is agnostic to any misalignment, stage motions in the left plane resulted in maximum amount of error. The corresponding errors in pixel units are also tabulated in Table 9.

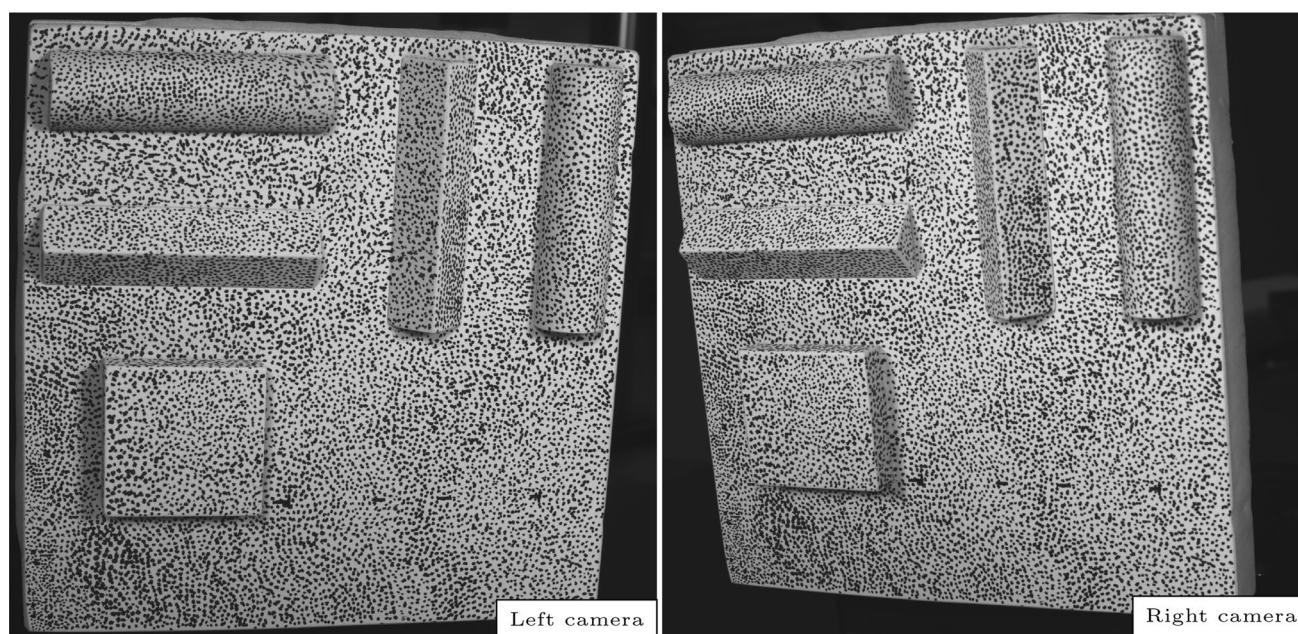
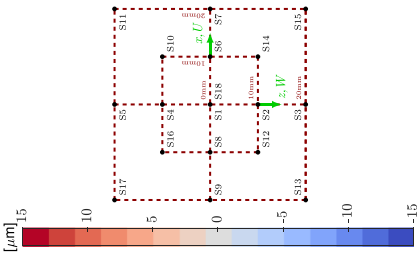


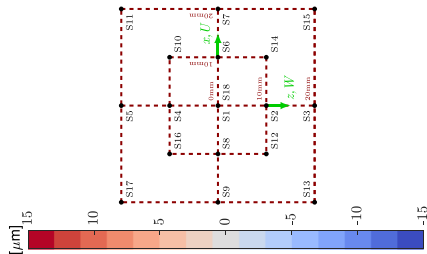
Fig. 17 Cropped 16 mm lens view at Step 17 for the (Left) camera and view from the (right) camera. Note the large perspective shift on the vertical triangle and the cylinder

Table 8 Maximum error map for each participant along with the step, denoted as “S”, at which the maximum error was observed. Abbreviation μ is used to denote mean value of displacements i.e., U_{DIC} , V_{DIC} , W_{DIC} , and A_{DIC} , subtracted from the corrected translation stage motion. Whereas σ denotes the standard deviation calculated from the AOI for a particular displacement field, U_{DIC} , V_{DIC} , W_{DIC} , and A_{DIC} . ΔA shows the residual field after removing the mean displacement calculated from DIC for steps with maximum error in $A(\mu \pm \sigma)$ columns. NOTE: All units in μm



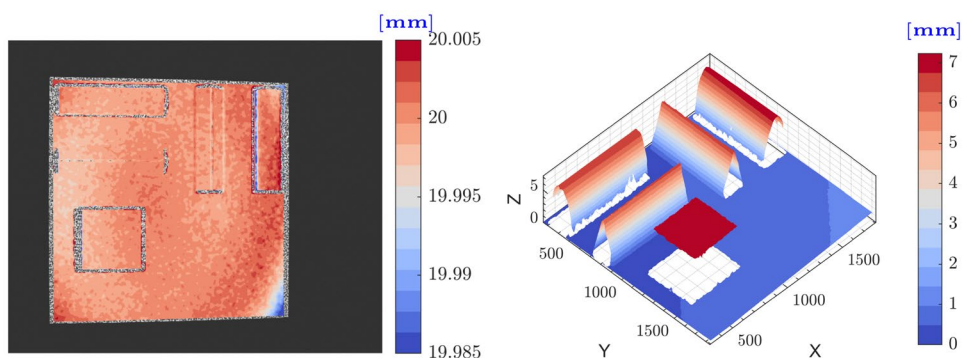
Group	$U_{(\mu \pm \sigma)}$	$V_{(\mu \pm \sigma)}$	$W_{(\mu \pm \sigma)}$	$A_{(\mu \pm \sigma)}$	35mm lens (ΔA)	16mm lens (ΔA)
1 (35mm)	$41.88 \pm 1.2(S: 13)$	$15.52 \pm 2.48(S: 15)$	$41.18 \pm 4.47(S: 15)$	$56.82 \pm 3.85(S: 13)$		
1 (16mm)	$43.99 \pm 3(S: 17)$	$21.89 \pm 3.14(S: 15)$	$34.8 \pm 3.56(S: 13)$	$53.24 \pm 4.89(S: 17)$		
2 (35mm)	$30.12 \pm 2.39(S: 15)$	$16.25 \pm 2.23(S: 15)$	$25.64 \pm 4.62(S: 11)$	$34.74 \pm 3.93(S: 11)$		
2 (16mm)	$26.94 \pm 2.35(S: 15)$	$18.27 \pm 2.24(S: 15)$	$20.74 \pm 5.25(S: 11)$	$31.59 \pm 4.12(S: 11)$		
3 (35mm)	$53.74 \pm 1.33(S: 13)$	$44.7 \pm 0.93(S: 11)$	$54.2 \pm 4.1(S: 13)$	$76.17 \pm 3.23(S: 13)$		
3 (16mm)	$50.26 \pm 2.4(S: 13)$	$60.05 \pm 2.13(S: 11)$	$43.62 \pm 2.98(S: 3)$	$65.07 \pm 4.62(S: 13)$		
4 (35mm)	$63.94 \pm 4.34(S: 13)$	$19.16 \pm 3.46(S: 11)$	$19.78 \pm 4.5(S: 3)$	$49.67 \pm 2.14(S: 9)$		
4 (16mm)	$89.89 \pm 8.62(S: 17)$	$28.64 \pm 10.46(S: 15)$	$51.1 \pm 5.84(S: 15)$	$52.52 \pm 2.93(S: 9)$		
5 (35mm)	$10.28 \pm 1.56(S: 15)$	$19.42 \pm 0.68(S: 11)$	$13.03 \pm 4.42(S: 15)$	$15.18 \pm 2.41(S: 13)$		
5 (16mm)	$15.92 \pm 1.67(S: 15)$	$34.07 \pm 1.46(S: 11)$	$52.43 \pm 4.66(S: 15)$	$51.01 \pm 2.19(S: 3)$		

Table 9 Maximum error map for each participant along with the step, denoted as “S”, at which the maximum error was observed. Abbreviation μ is used to denote mean value of displacements i.e., U_{DIC} , V_{DIC} , W_{DIC} , and A_{DIC} , subtracted from the corrected translation stage motion. Whereas σ denotes the standard deviation calculated from the AOI for a particular displacement field, U_{DIC} , V_{DIC} , W_{DIC} , and A_{DIC} . ΔA shows the residual field after removing the mean displacement calculated from DIC for steps with maximum error in $A(\mu \pm \sigma)$ columns. NOTE: All units in pixel. Scaling assumed to be 16.35pix/mm



Group	$U_{(\mu \pm \sigma)}$	$V_{(\mu \pm \sigma)}$	$W_{(\mu \pm \sigma)}$	$A_{(\mu \pm \sigma)}$	35mm lens (ΔA)	16mm lens (ΔA)
1 (35mm)	$0.68 \pm 0.02(S: 13)$	$0.25 \pm 0.04(S: 15)$	$0.67 \pm 0.07(S: 15)$	$0.93 \pm 0.06(S: 13)$		
1 (16mm)	$0.72 \pm 0.05(S: 17)$	$0.36 \pm 0.05(S: 15)$	$0.57 \pm 0.06(S: 13)$	$0.87 \pm 0.08(S: 17)$		
2 (35mm)	$0.49 \pm 0.04(S: 15)$	$0.27 \pm 0.04(S: 15)$	$0.42 \pm 0.08(S: 11)$	$0.57 \pm 0.06(S: 11)$		
2 (16mm)	$0.44 \pm 0.04(S: 15)$	$0.30 \pm 0.04(S: 15)$	$0.34 \pm 0.09(S: 11)$	$0.52 \pm 0.07(S: 11)$		
3 (35mm)	$0.88 \pm 0.02(S: 13)$	$0.73 \pm 0.02(S: 11)$	$0.89 \pm 0.07(S: 13)$	$1.25 \pm 0.05(S: 13)$		
3 (16mm)	$0.82 \pm 0.04(S: 13)$	$0.98 \pm 0.03(S: 11)$	$0.71 \pm 0.05(S: 3)$	$1.06 \pm 0.08(S: 13)$		
4 (35mm)	$1.05 \pm 0.07(S: 13)$	$0.31 \pm 0.06(S: 11)$	$0.32 \pm 0.08(S: 3)$	$0.81 \pm 0.04(S: 9)$		
4 (16mm)	$1.37 \pm 0.14(S: 17)$	$0.47 \pm 0.17(S: 15)$	$0.84 \pm 0.1(S: 15)$	$0.86 \pm 0.05(S: 9)$		
5 (35mm)	$0.17 \pm 0.03(S: 15)$	$0.32 \pm 0.01(S: 11)$	$0.21 \pm 0.07(S: 15)$	$0.25 \pm 0.04(S: 13)$		
5 (16mm)	$0.26 \pm 0.03(S: 15)$	$0.56 \pm 0.02(S: 11)$	$0.86 \pm 0.08(S: 15)$	$0.83 \pm 0.04(S: 3)$		

Fig. 18 Simulated images of the experiment for step 8. (Left) displacement map at step 8 and (Right) height map showing the shape



Discussion and Conclusion

The stereo-DIC challenge 1.0 provides a unique data set, with multiple calibration targets used and a highly controlled experimental setup. All known experimental error sources, excluding lens distortions, were controlled, and minimized with no evidence of heat waves or camera motion. Large translations were conducted of a complex shape to compare how well the codes were able to both reconstruct the shape and measure the translation. The DIC results were then compared to secondary measurements of a laser scanner for the shape and a nanometer precision stage for the displacement. Both full-field and averaged results were compared.

Five independent groups analyzed the images, including calibration of the system, using their own codes. All five codes were subset based DIC. Global codes were invited to participate but did not submit results. A sixth local code pulled out of the comparison during the analysis phase.

Overall, all five codes performed extremely well with 3D reconstruction and displacement errors of less than $\pm 80\mu\text{m}$ over a travel of $\pm 20\text{mm}$ which corresponds to a “full-scale” error of 0.2%. Typical errors are within $\pm 15\mu\text{m}$ which corresponds to ± 0.25 pixels at these scales. The test was challenging for DIC codes due to the complex shape and the large translation of the item. Of note was the ability of the DIC calibration to correct for rather large lens distortions in the 16mm lens and is shown by the similar results between the two lens types, even though the 16mm lens had more the 10 \times the lens distortions, the results showed only a modest increase in errors measured in the full-field standard deviation. The small error is particularly impressive because the object translates a large distance through the FOV exacerbating any uncorrected lens errors. The similarity in the results between lens focal lengths is important as lens selection is a key design component and often using shorter focal length lenses can improve the setup by positioning the cameras closer to the sample and decreasing the standoff. With experiments where the sample remains predominantly in the center of the FOV, these results seem to indicate that a well-calibrated system with wide-angle lenses

can be used without problems. Additionally, the choice of different matching criterion, Table 4 did not influence the results mainly because of well-controlled experimental setup and lighting.

In terms of closest coverage to the critical edges, group 2 was the leader with group 5 almost having nearly identical results. However, group 2 submission had a Moiré pattern which did not occur in group 5. By looking at the steps with maximum errors in Table 8, different groups had maximum errors at different locations in the measurement volume. This highlights the role of the calibration used by each group. It was also observed from the error in the absolute/magnitude fields that the frame with maximum error not only lay on the corners of FoV (Group 1,2,3,) but also on the horizontal and vertical baselines as reported by group 4 and group 5 (16mm). For the 35mm lens system, group 5 reported minimum errors. However, combining the errors from both lens systems, group 2 reported similar errors for both lenses and reported minimum combined errors in absolute magnitude field.

Two features seen in the full-field results of interest are PIB errors for all five codes. The PIB error source is a limiting factor in the shape reconstruction and the error magnitude, second only to the uncorrected lens distortions at the edges of the FOV. Group 2 also had moiré-like fringes in the results due to systematic errors coming from triangulation. The comparison with other groups enabled the development of the code and this problem was subsequently removed.

The shape of the item challenged all the codes in obtaining 100% coverage of the sample. Some of the missing data is expected due to stereo-occlusion between the left and right camera views, but other regions, including the peak of the triangle and the top of the cylinder as well as the triangle edges at the plate surface are not able to be matched with current subset-based methods. The lack of coverage emphasizes one drawback of DIC in that it is not able to obtain results all the way up to edges and/or discontinuities. Every group dropped results at these locations, as well as some other locations throughout the FOV due to other software metrics chosen as a data quality check. These most often involved a combination of correlation thresholds and

reprojection error constraints. The focus of the participants was on the measurement accuracy, so these parameters were not loosened to recover questionable data. Full coverage is most likely possible for all the codes, but at the expense of including data of lower quality.

We confirmed the accuracy and flexibility of DIC by comparing 5 independent analyses of a single data set. This paper is the first time a comparison has been done for Stereo-DIC between such a wide range of implementations. Several important hurdles were overcome for the comparison, most critically, getting a common coordinate system and aligning that with the stage motion was important and not trivial. Most of the errors measured in the preliminary analysis were simply coordinate system misalignment. After these problems were removed, DIC showed itself to be a flexible and accurate full-field measurement approach.

Some of the shortcomings of the current experimental effort will be rectified by an upcoming Stereo-DIC Challenge 2.0. The new challenge comparison will use a complex geometry in a tensile test to aim for comparing the strain results. Additionally, participants will be invited to the test to obtain their own calibration images.

Appendix A: Synthetic Images

Synthetic images were also created using a bespoke image simulator [25]. The stereo simulator used the calibrations from the 16mm and 35mm lens setups to create virtual cameras viewing the virtual plate. A nearly ideal speckle pattern was applied. The virtue of synthetic data is you know the information about both the shape and the displacement

exactly. Synthetic calibration images using a checkerboard with 10mm spacing, a dot grid 14×10-10mm spacing and a two-level grid (target 106-10) with 10mm dot spacing, 2.2mm diameter dots and 2mm level change were created and are stored with the challenge images. The plate was translated exact amounts with the synthetic sample made to the exact drawing specifications in Fig. 2. Figure 18 shows a typical DIC result at Step 8 for the synthetic data. This data is available in the repository and researchers are encouraged to use this for investigation of Stereo-DIC algorithms.

Appendix B: Laser Line Probe Specifications

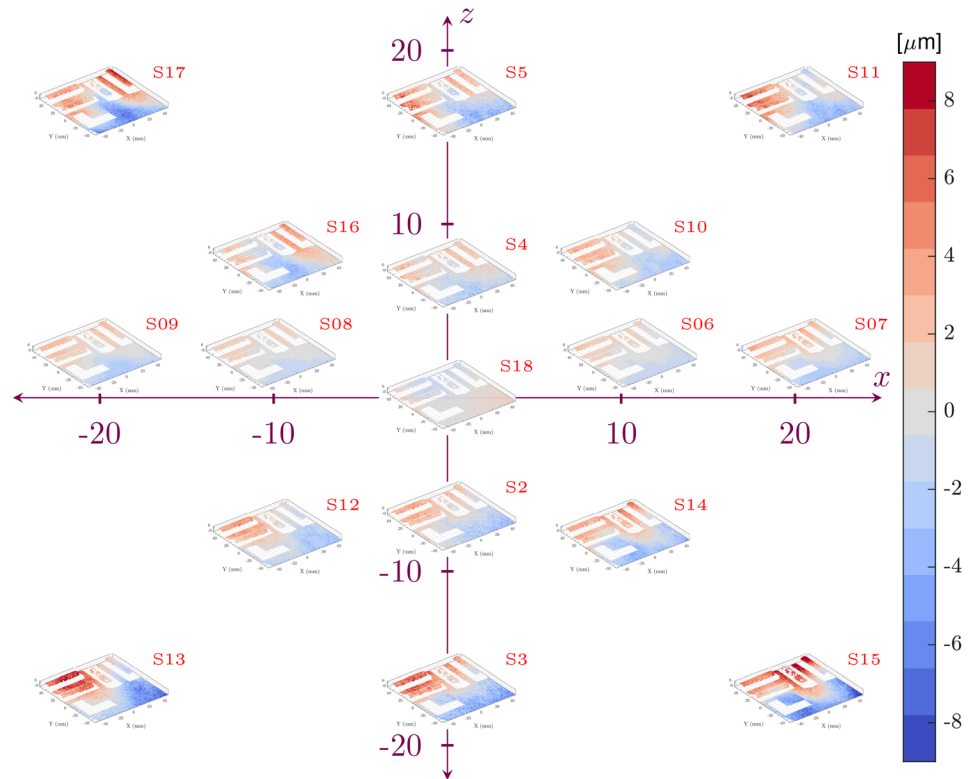
Table 10 Specifications of Faro Edge Laser scanner probe

Specification	Values
Accuracy	$\pm 25\mu\text{m}$
Repeatability	$25\mu\text{m}, 2\sigma(0.001\text{in})$
Stand-off	115mm(4.5in)
Depth of Field	115mm(4.5in)
Effective Scan Width	Near-field 80mm, Far-field 150mm
Points per line	2000 points/line
Minimum Point Spacing	$40\mu\text{m}, (0.0015\text{in})$
Scan Rate	280 frames/second, $280\text{fps} \times 2000$ points/line = 560000 points/sec
Laser	Class 2M
Weight	485g (1.1lb)

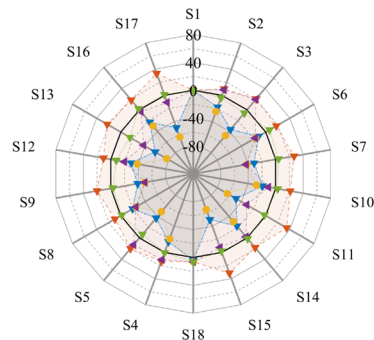
Appendix C: A Displacement

35mm Lens

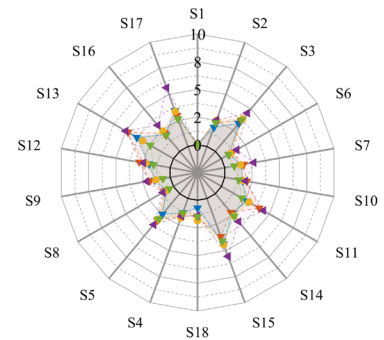
Fig. 19 Group 1: 35mm Lens, A displacement. **a** Residual plots of A at all steps. Axis values indicate the displacement in mm. Colorbar scale is in μm . **b** Mean, μ , of the ROI at each step. **c** Standard deviation, σ , of the ROI at each step



(a) Residual fields of A at each step.

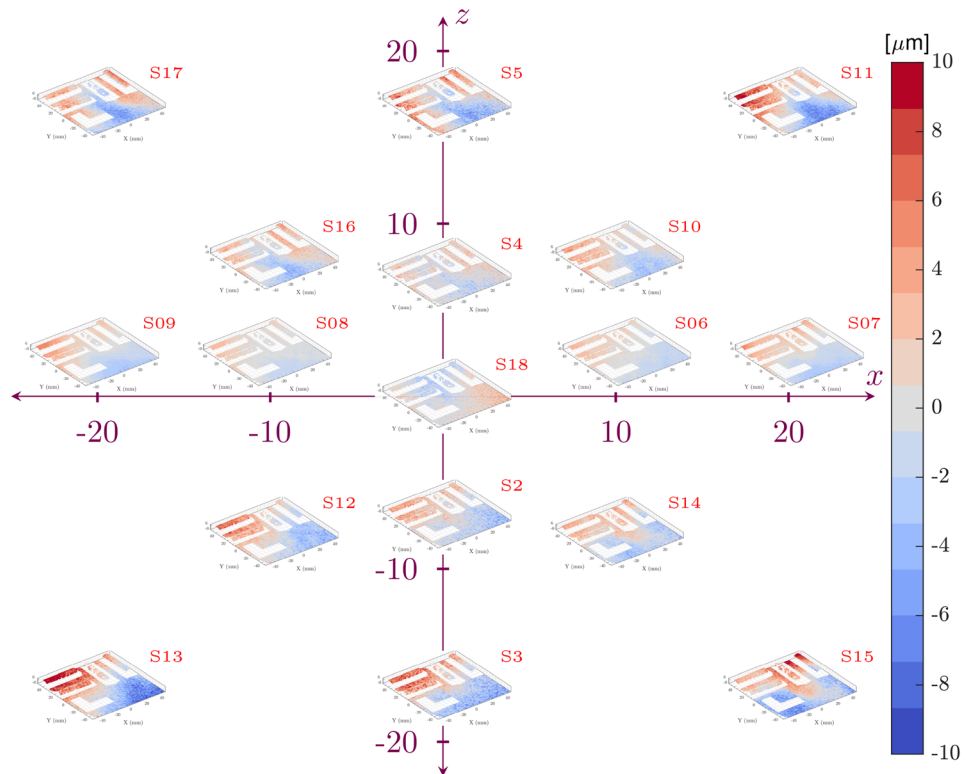


(b) $\mu(A_{\text{stage}} - A_{\text{DIC}})$

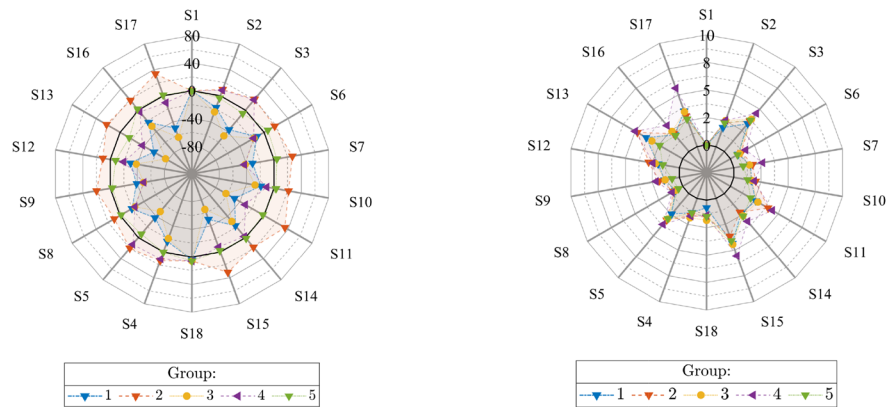


(c) $\sigma(A_{\text{DIC}})$

Fig. 20 Group 2: 35mm Lens, A displacement. **a** Residual plots of A at all steps. Axis values indicate the displacement in mm. Colorbar scale is in μm . **b** Mean, μ , of the ROI at each step. **c** Standard deviation, σ , of the ROI at each step



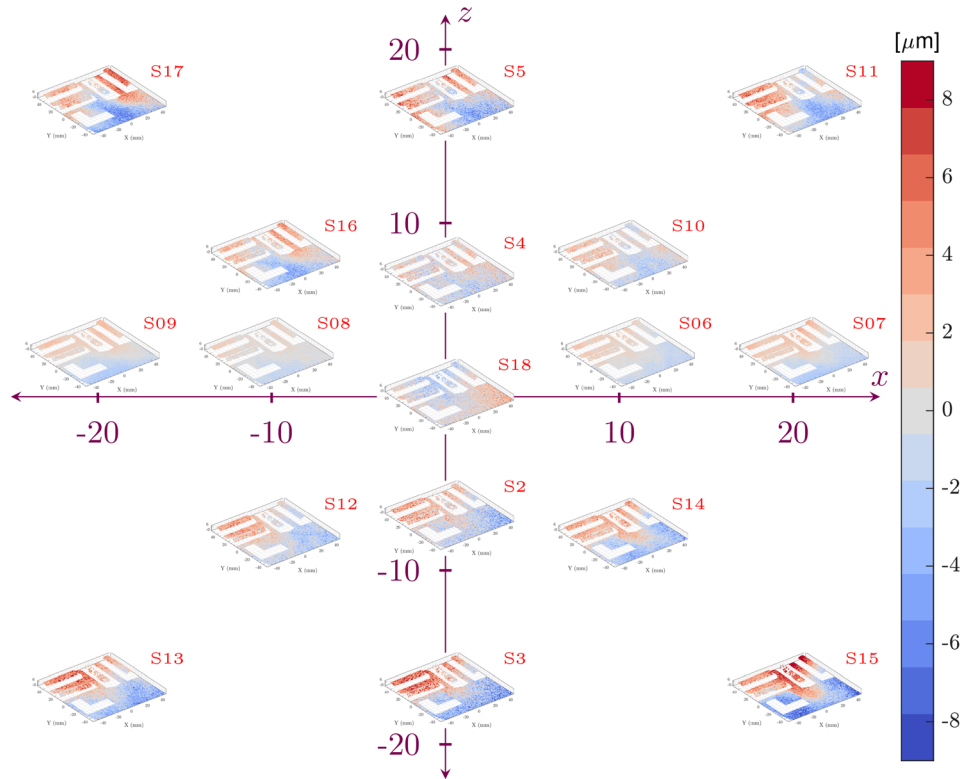
(a) Residual fields of A at each step.



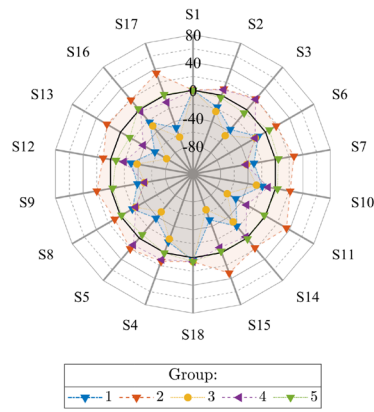
(b) $\mu(A_{\text{stage}} - A_{\text{DIC}})$

(c) $\sigma(A_{\text{DIC}})$

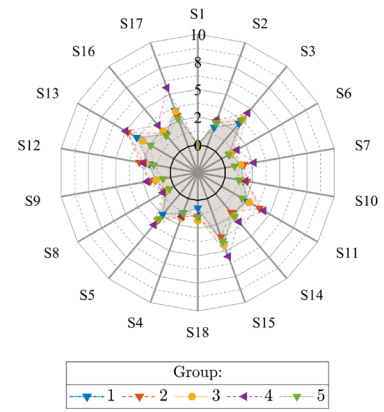
Fig. 21 Group 3: 35mm Lens, A displacement. **a** Residual plots of A at all steps. Axis values indicate the displacement in mm. Colorbar scale is in μm . **b** Mean, μ , of the ROI at each step. **c** Standard deviation, σ , of the ROI at each step



(a) Residual fields of A at each step.

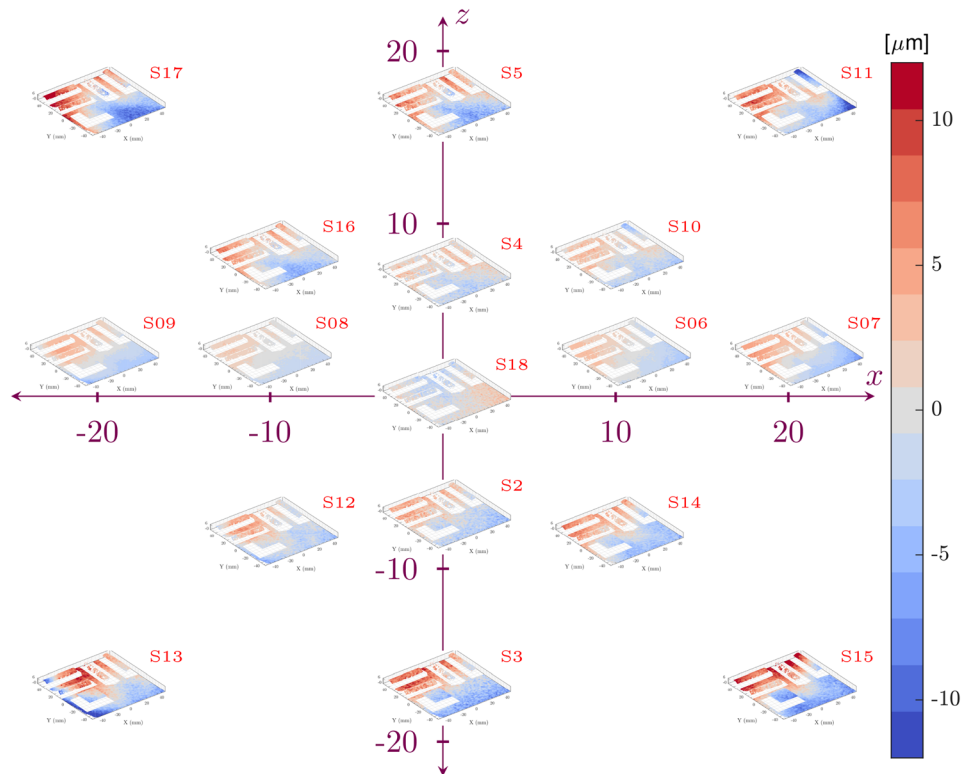


(b) $\mu(A_{\text{stage}} - A_{\text{DIC}})$

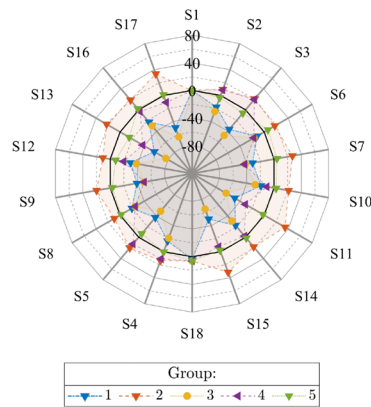


(c) $\sigma(A_{\text{DIC}})$

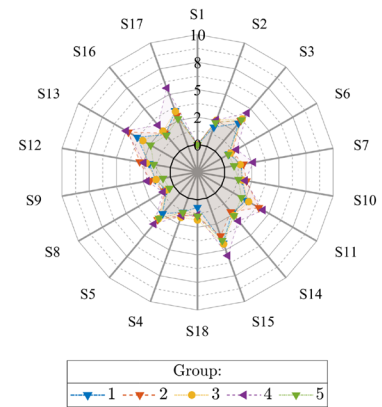
Fig. 22 Group 4: 35mm Lens, A displacement. **a** Residual plots of A at all steps. Axis values indicate the displacement in mm. Colorbar scale is in μm . **b** Mean, μ , of the ROI at each step. **c** Standard deviation, σ , of the ROI at each step



(a) Residual fields of A at each step.

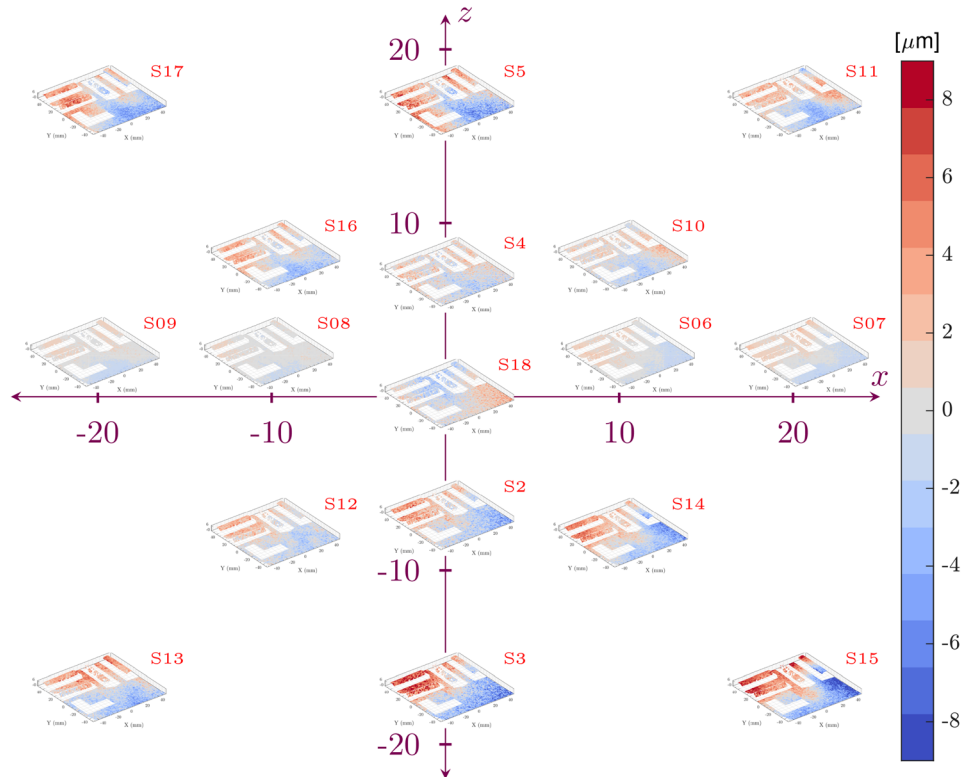


(b) $\mu(A_{\text{stage}} - A_{\text{DIC}})$

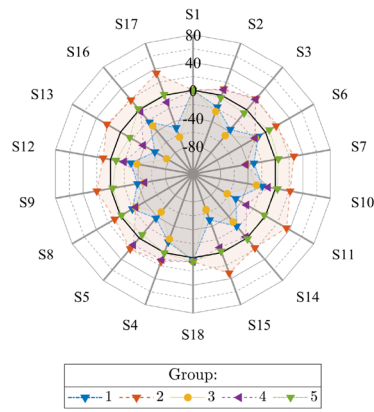


(c) $\sigma(A_{\text{DIC}})$

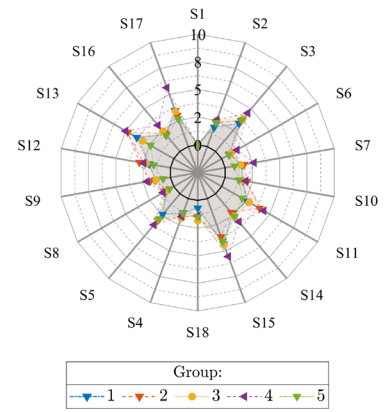
Fig. 23 Group 5: 35mm Lens, A displacement. **a** Residual plots of A at all steps. Axis values indicate the displacement in mm. Colorbar scale is in μm . **b** Mean, μ , of the ROI at each step. **c** Standard deviation, σ , of the ROI at each step



(a) Residual fields of A at each step.

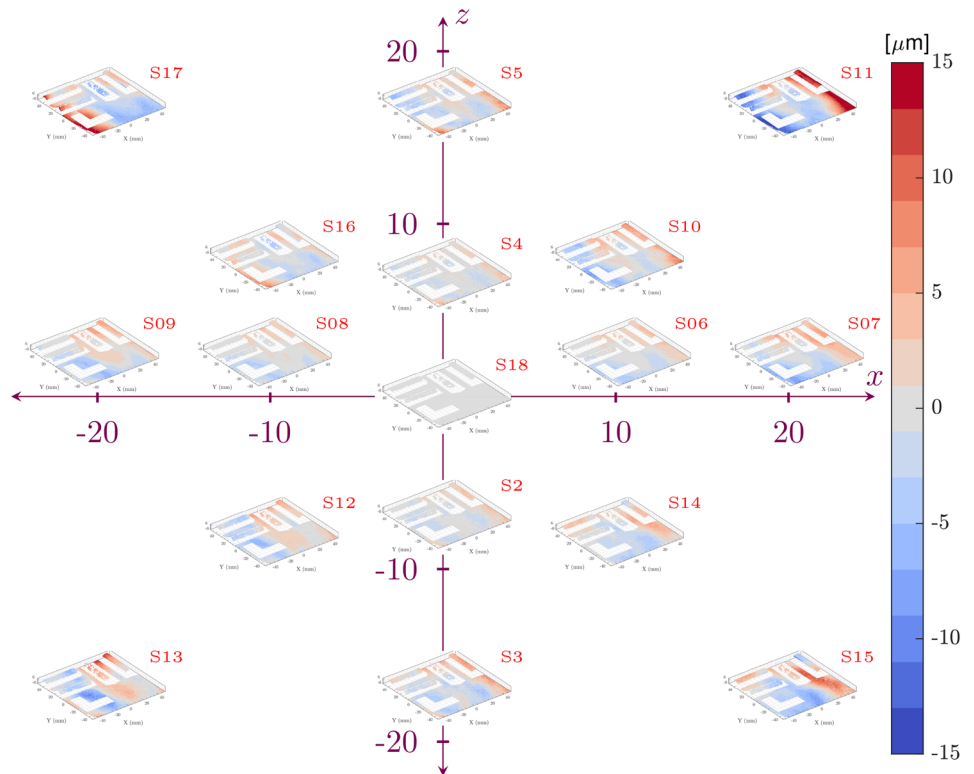


(b) $\mu(A_{\text{stage}} - A_{\text{DIC}})$

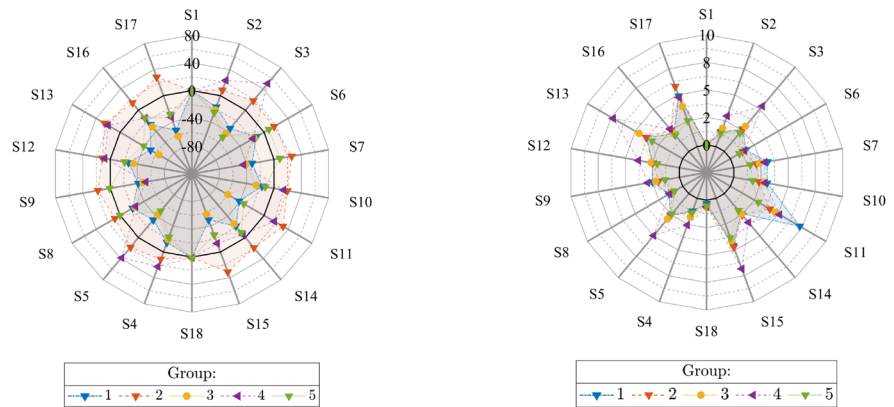


(c) $\sigma(A_{\text{DIC}})$

Fig. 24 Group 1: 16mm Lens, A displacement. **a** Residual plots of A at all steps. Axis values indicate the displacement in mm. Colorbar scale is in μm . **b** Mean, μ , of the ROI at each step. **c** Standard deviation, σ , of the ROI at each step



(a) Residual fields of A at each step.

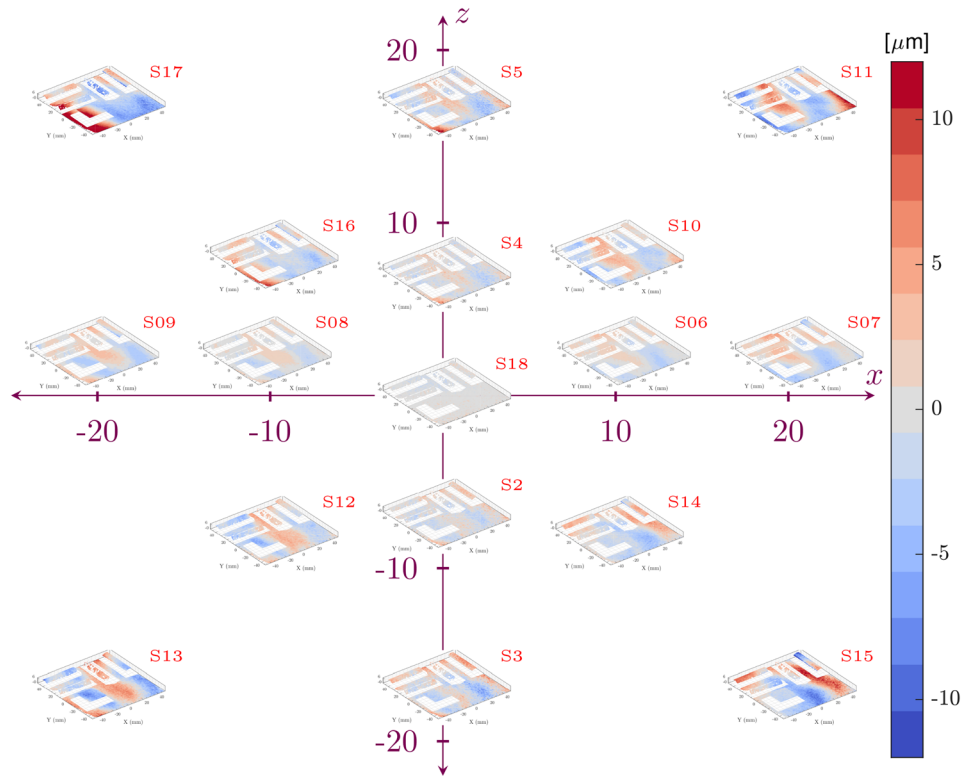


(b) $\mu(A_{\text{stage}} - A_{\text{DIC}})$

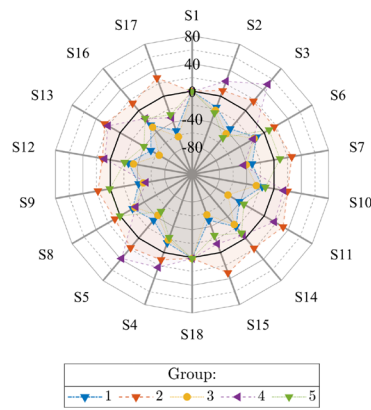
(c) $\sigma(A_{\text{DIC}})$

16mm Lens

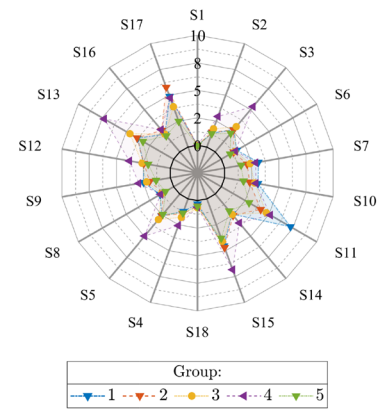
Fig. 25 Group 2: 16mm Lens, A displacement. **a** Residual plots of A at all steps. Axis values indicate the displacement in mm. Colorbar scale is in μm . **b** Mean, μ , of the ROI at each step. **c** Standard deviation, σ , of the ROI at each step



(a) Residual fields of A at each step.

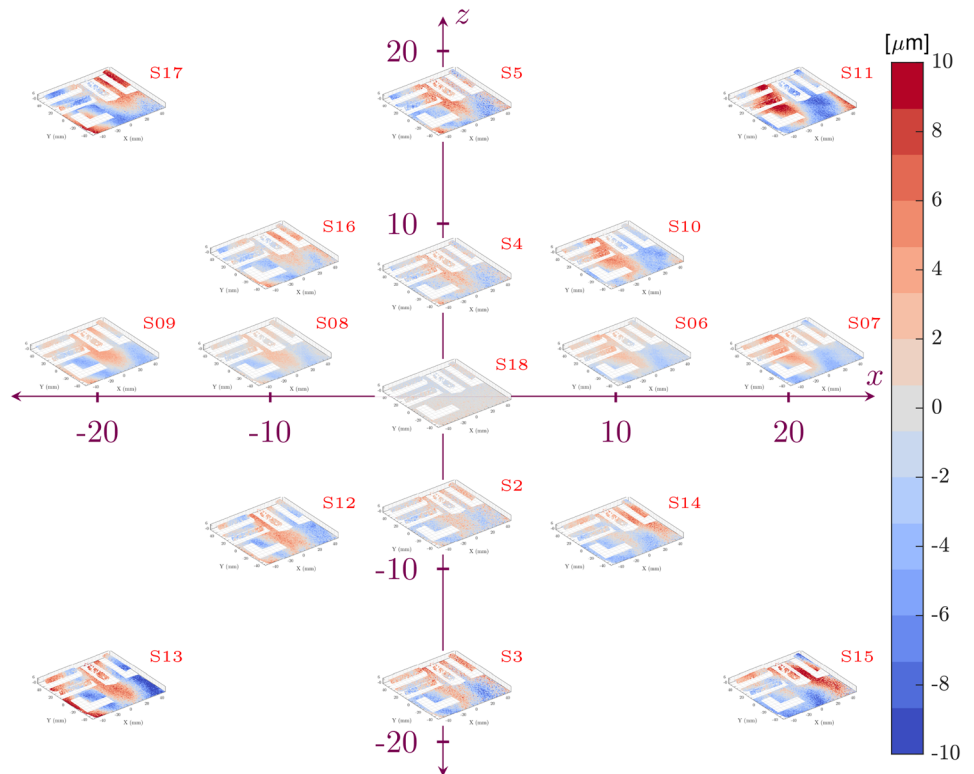


(b) $\mu(A_{\text{stage}} - A_{\text{DIC}})$

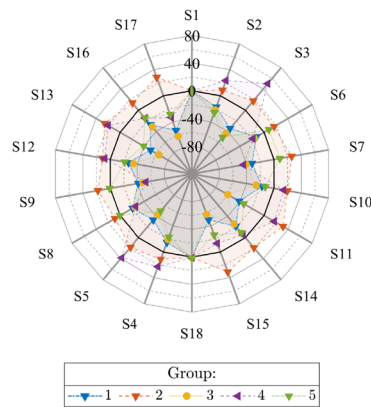


(c) $\sigma(A_{\text{DIC}})$

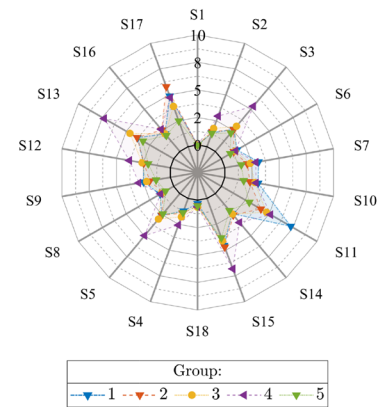
Fig. 26 Group 3: 16mm Lens, A displacement. **a** Residual plots of A at all steps. Axis values indicate the displacement in mm. Colorbar scale is in μm . **b** Mean, μ , of the ROI at each step. **c** Standard deviation, σ , of the ROI at each step



(a) Residual fields of A at each step.

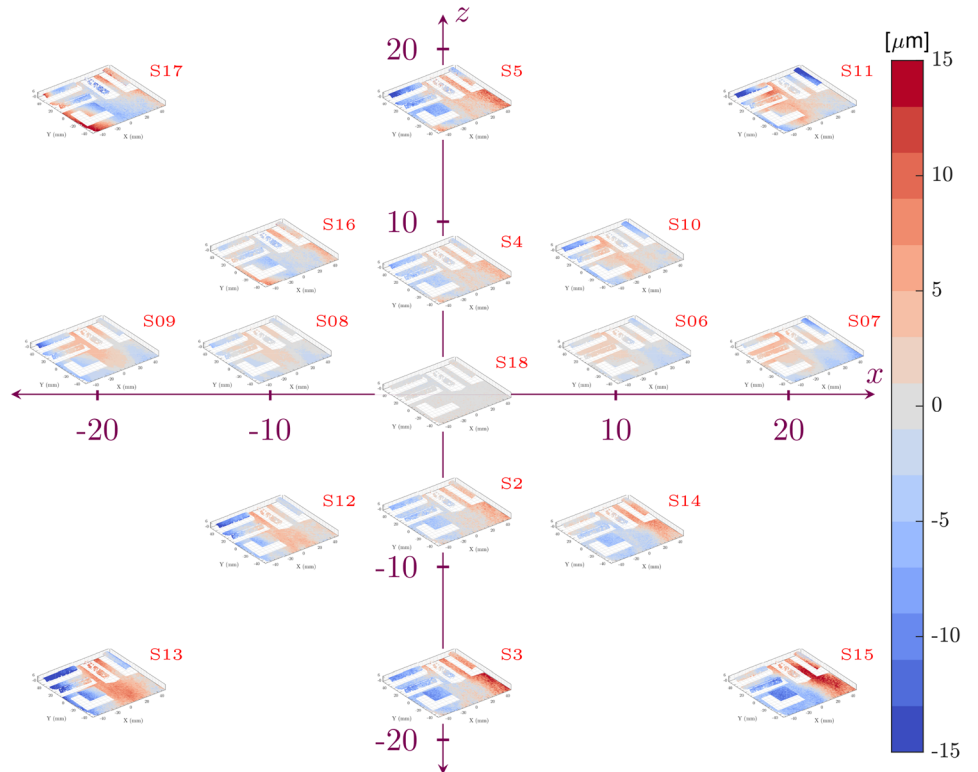


(b) $\mu(A_{\text{stage}} - A_{\text{DIC}})$

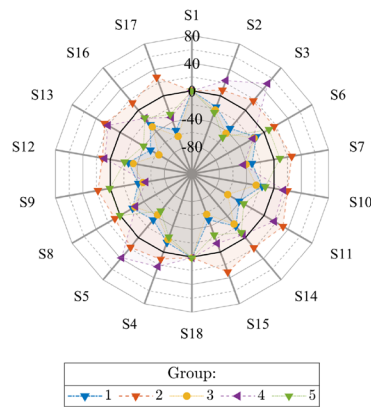


(c) $\sigma(A_{\text{DIC}})$

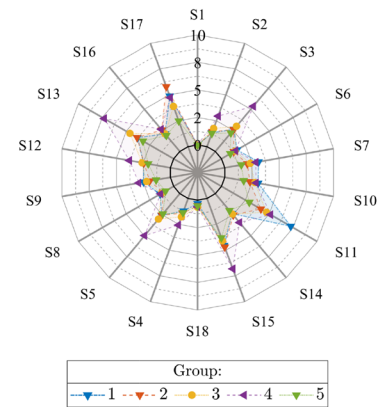
Fig. 27 Group 4: 16mm Lens, A displacement. **a** Residual plots of A at all steps. Axis values indicate the displacement in mm. Colorbar scale is in μm . **b** Mean, μ , of the ROI at each step. **c** Standard deviation, σ , of the ROI at each step



(a) Residual fields of A at each step.

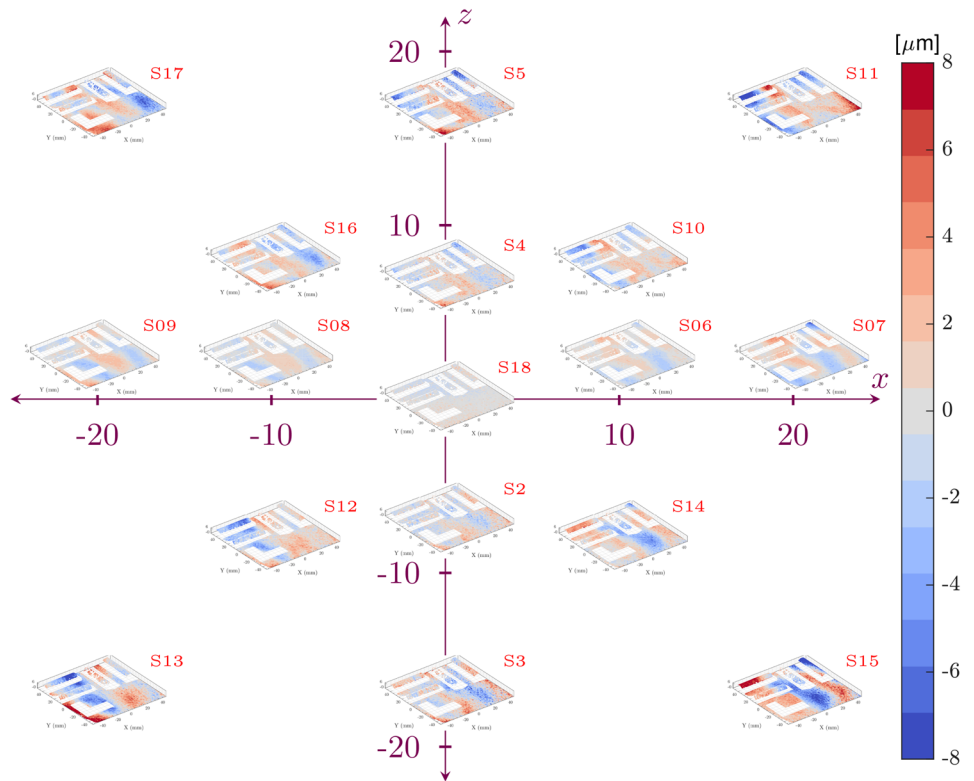


(b) $\mu(A_{\text{stage}} - A_{\text{DIC}})$

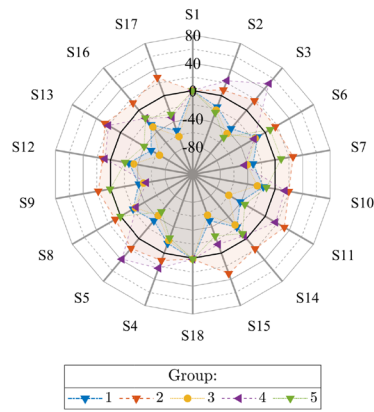


(c) $\sigma(A_{\text{DIC}})$

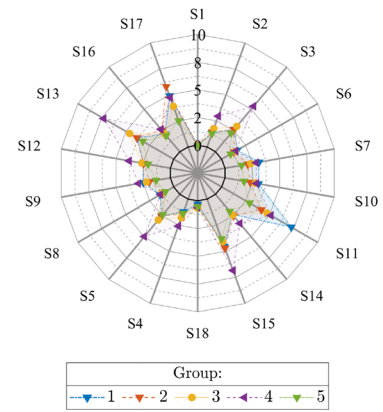
Fig. 28 Group 5: 16mm Lens, A displacement. **a** Residual plots of A at all steps. Axis values indicate the displacement in mm. Colorbar scale is in μm . **b** Mean, μ , of the ROI at each step. **c** Standard deviation, σ , of the ROI at each step



(a) Residual fields of A at each step.



(b) $\mu(A_{\text{stage}} - A_{\text{DIC}})$



(c) $\sigma(A_{\text{DIC}})$

Acknowledgements Sandia National Laboratories is a multimission laboratory managed and operated by National Technology and Engineering Solutions of Sandia, LLC, a wholly owned subsidiary of Honeywell International Inc., for the U.S. Department of Energy's National Nuclear Security Administration under contract DE-NA0003525.

Declarations

Conflict of Interest The authors declare that they have no conflict of interest.

Open Access This article is licensed under a Creative Commons Attribution 4.0 International License, which permits use, sharing, adaptation, distribution and reproduction in any medium or format, as long as you give appropriate credit to the original author(s) and the source, provide a link to the Creative Commons licence, and indicate if changes were made. The images or other third party material in this article are included in the article's Creative Commons licence, unless indicated otherwise in a credit line to the material. If material is not included in the article's Creative Commons licence and your intended use is not permitted by statutory regulation or exceeds the permitted use, you will need to obtain permission directly from the copyright holder. To view a copy of this licence, visit <http://creativecommons.org/licenses/by/4.0/>.

References

- Jones EM, Iadicola MA et al (2018) A good practices guide for digital image correlation. *International Digital Image Correlation Society* 10
- Reu PL, Toussaint E, Jones E, Bruck HA, Iadicola M, Balcaen R et al (2018) DIC challenge: developing images and guidelines for evaluating accuracy and resolution of 2D analyses. *Exp Mech* 58:1067–1099
- Reu PL, Blaysat B, Andò E, Bhattacharya K, Couture C, Couty V et al (2022) DIC Challenge 2.0: developing images and guidelines for evaluating accuracy and resolution of 2D analyses: focus on the metrological efficiency indicator. *Exp Mech* 62(4):639–654
- Bossuyt S (2013) Optimized patterns for digital image correlation. In: *Imaging Methods for Novel Materials and Challenging Applications*, Volume 3. Springer. p. 239–248
- Chen Z, Shao X, Xu X, He X (2018) Optimized digital speckle patterns for digital image correlation by consideration of both accuracy and efficiency. *Appl Opt* 57(4):884–893
- Su Y, Zhang Q, Gao Z (2017) Statistical model for speckle pattern optimization. *Opt Express* 25(24):30259–30275
- Pan B, Wu D, Yu L (2012) Optimization of a three-dimensional digital image correlation system for deformation measurements in extreme environments. *Appl Opt* 51(19):4409–4419
- Hassan GM, MacNish C, Dyskin A, Shufrin I (2016) Digital image correlation with dynamic subset selection. *Opt Lasers Eng* 84:1–9
- Li BJ, Wang Q, Duan DP, Chen JA (2017) Modified digital image correlation for balancing the influence of subset size choice. *Opt Eng* 56(5):054104
- Reu P (2013) A study of the influence of calibration uncertainty on the global uncertainty for digital image correlation using a Monte Carlo approach. *Exp Mech* 53(9):1661–1680
- Liu X, Li Z, Zhong K, Chao Y, Miraldo P, Shi Y (2018) Generic distortion model for metrology under optical microscopes. *Opt Lasers Eng* 103:119–126
- Pan B, Shi W, Lubineau G (2015) Effect of camera temperature variations on stereo-digital image correlation measurements. *Appl Opt* 54(34):10089–10095
- Hu Z, Xie H, Lu J, Wang H, Zhu J (2011) Error evaluation technique for three-dimensional digital image correlation. *Appl Opt* 50(33):6239–6247
- Wang YQ, Sutton M, Ke XD, Schreier H, Reu P, Miller T (2011) On error assessment in stereo-based deformation measurements. *Exp Mech* 51(4):405–422
- Ke XD, Schreier H, Sutton M, Wang Y (2011) Error assessment in stereo-based deformation measurements. *Exp Mech* 51(4):423–441
- Zhong F, Shao X, Quan C (2019) A comparative study of 3D reconstruction methods in stereo digital image correlation. *Opt Lasers Eng* 122:142–150
- Schreier HW, Sutton MA (2002) Systematic errors in digital image correlation due to undermatched subset shape functions. *Exp Mech* 42(3):303–310
- Wang Z, Li H, Tong J, Ruan J (2007) Statistical analysis of the effect of intensity pattern noise on the displacement measurement precision of digital image correlation using self-correlated images. *Exp Mech* 47(5):701–707
- Couto PRG, Damasceno JC, Oliveira SD, Chan W (2013) Monte Carlo simulations applied to uncertainty in measurement. *Theory and applications of Monte Carlo simulations*, p 27–51
- Di Leo G, Liguori C, Paolillo A (2011) Covariance propagation for the uncertainty estimation in stereo vision. *IEEE Trans Instrum Meas* 60(5):1664–1673
- Siebert T, Becker T, Splitthof K, Neumann I, Krupka R (2007) High-speed digital image correlation: error estimations and applications. *Opt Eng* 46(5):051004
- Haddadi H, Belhabib S (2008) Use of rigid-body motion for the investigation and estimation of the measurement errors related to digital image correlation technique. *Opt Lasers Eng* 46(2):185–196
- Nansteel MW, Chen CCT (2009) Digital image correlation: A measurement tool for the study of explosive effects. In: *2009 Ieee Conference on Technologies for Homeland Security*. IEEE, p 234–241
- Jones E, Reu P (2018) Distortion of digital image correlation (DIC) displacements and strains from heat waves. *Exp Mech* 58(7):1133–1156
- Balcaen R, Wittevrongel L, Reu P, Lava P, Debruyne D (2017) Stereo-DIC calibration and speckle image generator based on FE formulations. *Exp Mech* 57(5):703–718

Publisher's Note Springer Nature remains neutral with regard to jurisdictional claims in published maps and institutional affiliations.